High-resolution structures and conformational dynamics of RNA origami during folding

Ebbe Andersen (esa@inano.au.dk)
Aarhus University https://orcid.org/0000-0002-6236-8164
Ewan McRae
Aarhus University
Helena Rasmussen
Aarhus University
Jianfang Liu
Lawrence Berkeley National Laboratory
Andreas Bøggild
Aarhus University
Michael Nguyen
Aarhus University
Nestor Vallina
Aarhus University
Thomas Boesen
Aarhus University
Jan Skov Pedersen
iNANO, Aarhus University https://orcid.org/0000-0002-7768-0206
Gang (Gary) Ren
Lawrence Berkeley National Laboratory https://orcid.org/0000-0002-8036-2321
Cody Geary
Aarhus University

Article

Keywords:

Posted Date: September 1st, 2022

DOI: https://doi.org/10.21203/rs.3.rs-1182359/v1

High-resolution structures and conformational dynamics of RNA origami during folding

Ewan K.S. McRae[1], Helena Østergaard Rasmussen[1,2], Jianfang Liu[4], Andreas Bøggild[1], Michael T.A. Nguyen[1], Nestor Sampedro Vallina[1], Thomas Boesen[1,3], Jan Skov Pedersen[1,2], Gang Ren[4], Cody Geary[1], Ebbe Sloth Andersen[1,3,*]

[1]Interdisciplinary Nanoscience Center (iNANO), Gustav Wieds Vej 14, Aarhus University, DK-8000 Aarhus, Denmark.
[2]Department of Chemistry, Gustav Wieds Vej 14, Aarhus University, DK-8000 Aarhus, Denmark.
[3]Department of Molecular Biology and Genetics, Gustav Wieds Vej 14, Aarhus University, DK-8000 Aarhus, Denmark.
[4]The Molecular Foundry, Lawrence Berkeley National Laboratory, 1 Cyclotron Road, MS 67R2206, Berkeley CA 94720-8197.

*Corresponding author. Email: esa@inano.au.dk

Cotranscriptional folding of RNA is a fundamental self-assembly process of nature[1], important for the biological assembly of complex molecular machines like the ribosome[2]. Inspired by this folding process, we developed the cotranscriptional RNA origami design method to efficiently produce RNA nanostructures by enzymatic synthesis[3,4], advantageous for large-scale production *in vitro*[5] or expression *in vivo*[6-8]. However, advancing this technology further will require high-resolution characterization and a better understanding of the cotranscriptional folding process. Here, we use cryogenic electron microscopy to study a panel of RNA origami structures at local resolutions up to 3.4 Å, revealing details of kissing loop and crossover structural modules used to compose RNA origami. The derived structural parameters are used to reduce internal strain and global twist to obtain more ideal shapes. In three-dimensional bundle designs, we discover a novel kinetic folding trap that forms during cotranscriptional folding, and is only released 6-8 hours after transcription. Finally, pushing both scale and complexity, we design the first multi-domain RNA origami and characterize the conformational variability of its domains by individual particle electron tomography. Our results improve understanding of RNA structure, dynamics, and folding, providing a basis for future applications of cotranscriptional folding in RNA medicine[9] and synthetic biology[10,11].

The use of nucleic acids as a construction material for programmable self-assembly of nanoscale shapes was originally suggested 40 years ago by Ned Seeman[12]. DNA molecules were initially used for implementing geometrical shapes and extended lattices[13,14]. Even though RNA molecules are more fragile than DNA, they were used to build early nanostructures[15], which developed into a field of its own by using naturally occurring RNA tertiary motifs as modular building blocks[16]. A breakthrough in DNA nanotechnology came with the introduction of the DNA origami method, which improved assembly scale and yield by folding a long single-stranded DNA using a large set of short DNA strands[17]. The ability of DNA origami to design arbitrary shapes and to be used as a breadboard for organizing molecular components rendered it an important tool for nanotechnology[18].

Inspired by DNA origami, we developed RNA origami as a single-stranded architecture by implementing RNA double crossover (DX) and RNA kissing loop (KL) motifs[3]. RNA origami was shown to be compatible with cotranscriptional folding and has since been improved with optimized structure and sequence design software[4]. RNA origami has previously been characterized mainly using methods in which the sample is adhered to a surface, such as atomic force microscopy (AFM) or negative stain transmission electron microscopy (NS-TEM). However, the forces keeping the RNA stuck to the surface in these methods can distort the solution structure of the RNA, and these methods are limited in the resolution of structural detail they can attain.

Cryogenic electron microscopy (cryo-EM) has been used to characterize RNA nanostructures, but generally have resulted in low resolution maps that only provide a general sense of the global structure[6,7,19-27]. The field of cryo-EM has now advanced to the stage where a higher resolution can be readily achieved, and we have witnessed a recent surge of high-resolution RNA-only cryo-EM structures where the deep and shallow grooves are clearly resolved[28-32]. For DNA nanostructures the shift of characterization tools from AFM to cryo-EM enabled 3D characterization of larger and more complex DNA origami[33] at increasing resolution[34], in which the twisting and bending observed allowed for adjustments to the design parameters to control their global shape[35].

Here, we present a suite of RNA origami studied by cryo-EM and reconstructed to high resolution that allows us to build atomistic models of RNA origami. The combination of cryo-EM single particle analysis, individual particle electron tomography (IPET) and small-angle X-ray scattering (SAXS) data allows us to present detailed analysis of the dynamic movements of RNA, and reveal complex, slow maturation processes.

Design of RNA origami for cryo-EM analysis

Using our recently developed ROAD software[4] we designed a panel of RNA origami structures for cryo-EM analysis (Supplementary Table 1-8). The designs were carefully chosen to test the structural assumptions that we make in RNA origami design, which has previously allowed us to achieve kilobase-sized nanoscaffolds, albeit at decreasing yield for larger structures[4]. The first assumption is that a DX, with an integer number of full-turns between crossovers, forces the helices to be parallel – even though a single crossover found in natural RNA structures typically places two helical segments at an angle θ of ~ 45 ° (**Fig. 1a,b**)[36]. The second assumption is that a KL motif corresponds to 9 bps of A-form helix, and can be placed on a continuous helical segment between two crossovers. A third assumption is that the number of bps between two crossovers connecting three adjacent helices, named a dovetail (DT) seam, dictates the angle φ between adjacent helices (**Fig. 1c,d**). Any deviation from these assumptions will cause distortions that will propagate throughout the structure and may limit fidelity and yield of RNA origami designs.

Our point of departure is the 5-helix tile (5HT) that has previously been shown to fold in high yield[4]. The 5HT-A design has a DT pattern of -2, +11, -2 bp, which corresponds to φ angles of 155 °, 220 °, 155 ° (**Fig. 1e,f**). In theory, moving a crossover position by increments of 11 bp should not affect the φ angle. We test this by the 5HT-B design with a DT pattern of -2, -11, -2 bp, where the DX between H3 and H4 is moved 22 bps. To test global twist we extended 5HT-B into a wider tile called 5HT-B-3X. To develop 3D shapes, we design 6-helix bundles (6HB) by utilizing a -3 bp seam pattern to orient the helices at φ angles of 122 °, resulting in a hexagonal cross-section (**Fig. 1g,h**). Variants of the bundle design allow us to explore different cotranscriptional folding strategies. Finally, we explore the use of a branched kissing loop (bKL) module[7] to combine two 5HT and a 6HB, forming a distinctive 16-helix "satellite" (16HS) shape of 1,832 nt (**Fig. 1i**). The 16HS design is the first three-domain RNA origami structure and has a very complex strand path making it a good candidate for testing the design of 3D RNA origami. The strand paths were chosen based on folding path analysis[4] and our current understanding of the cotranscriptional folding and maturation process (**Fig. 1j**). All designs were synthesized, transcribed, purified and analyzed by cryo-EM (see Methods, Extended Data Fig. 1 and Supplementary Table 9).

5-helix sheets with twists and bends

The cryo-EM reconstruction of the 5HT-A design reached an overall resolution of 4.1 Å with local resolutions up to 3.4 Å (Supplementary Video 1). Compared to our designed model, we observed bending of helices between crossovers and twisting at junctions (**Fig. 2a**). The A-form helices have

average helical rise and twist of 2.7 Å and 33.2 ° per bp, which is close to the expected values of 2.8 Å and 32.7 °, respectively (Extended Data Fig. 2e). However, we observe overtwisting localized to the 2-bp seams, where the average helical twist is 35.6 ° per bp. While H1, H2 and H4 have curved helical axes, the central helix, H3, has two distinctive kinks at the most interior crossovers and is otherwise straight (Extended Data Fig. 2d). Measurements of the φ angles show deviation from the ideal values (Extended Data Fig. 3 and 5) and 3D variability analysis shows flexibility of helix ends, φ angles and θ angles (Supplementary Video 2).

The slight change in topology of 5HT-B resulted in a substantial difference in the alignment of helices (**Fig. 2b**). H3 appears bent (155 °), compared to the relatively straight H3 from 5HT-A (Extended Data Fig. 2d). However, 5HT-B had a similar left-handed twist between adjacent DT seams (or seam twist) as 5HT-A (Extended Data Fig. 3c). 5HT-B-3X was used to investigate the seam twist further since an extended structure should average out local deformations (**Fig. 2c**). 5HT-B-3X tile has a left-handed twist of -26 ° (Extended Data Fig. 3d and 5d) and a global bend that creates two distinct sides, one with more exposed surface area — which explains the preferential landing of larger RNA origami tiles that we previously observed by negative stain TEM and AFM[4].

Kissing loop motif and twist correction

Local refinement of the 5HT-A reveals the KL motif at 3.7-Å resolution with distinct features as compared to earlier KL structures determined by crystallography[37-39] and NMR[40-42]. The KL is composed of two bulged purines (A1 and A2), 6 nucleotides that form bps with a complementary KL, and an unpaired purine (A3). We find that the A1 and A3 form a trans WC-WC bp (**Fig. 2e**) that stacks between the A-form and KL double helices. A1 and A2 are not in the bulged-out conformation observed in crystal structures[37-39] but rather the A2 nucleotides form a base stack within the major groove, further stabilized by hydrogen bonds from the NH_2 group of one A2 to the 2'OH of the other (**Fig. 2f**). Our model indicates that both A1 and A2 nucleotides adopt a C2'-endo sugar pucker on both sides of the KL dimer. Of the 41 KLs reconstructed from 8 independent datasets (not counting 12 KLs from 5HT-B-3X) we observe what appears to be bulged out A1/A2 in three KLs of our maps (Extended Data Fig. 6).

The data further shows that the central KL bp stack is overtwisted and compressed compared to the rest of the structure with average helical rise and twist of 2.5 Å and 31 ° per bp, respectively (Extended Data Fig. 2e). We find that a KL motif can be approximated as 8 bp of continuous A-form helix, whereas in our current designs we approximate them as 9 bp. This

observation agrees with recent X-ray studies on a synthetically constructed bKL motif that found the same overtwisting[43]. Based on this observation we designed a twist-corrected version of 5HT-A, where we added an extra bp in each KL-containing helix segment. The cryo-EM reconstruction had a more ideal shape with a positive average seam twist of +15 ° (compared to –28 ° for 5HT-A) and average φ angles of 156 ° and 236 °, which are very close to ideal values of 155 ° and 220 °, and with less in and out of plane θ bending (**Fig. 2d**, Extended Data Fig. 3b and 5). This demonstrates how cryo-EM derived parameters can be used to iteratively optimize RNA origami shapes.

Tertiary motif of crossover junctions

The crossover junctions of 5HT-A reach local resolution of 3.4 Å (Extended Data Fig. 2a) and are thus one of the most rigid parts of the RNA origami due to continuous base stacking across the junctions. The DXs across multiple structures are found to have average θ angles of 11.3 +/- 7.3 ° (**Fig. 2g**) and we often observe an alternating pattern of θ angles compatible with bending in and out of the plane (Extended Data Fig. 5c). The four instances in 5HT-A of junctions with 2-bp DTs show remarkable similarity, indicating that their structure can be defined as a rigid module and used as a building block for future designs.

Analysis of the crossovers of 5HT-A revealed that 9 out of 32 of the four-way junction nucleotides (J1-4) adopt C2'-endo sugar pucker, one per crossover and one crossover with two (**Fig. 2h**). All the C2'-endo nucleotides are at the 5' end of the strand entering the crossover (J1 and J3) and fall into the 1b rotameric classification[44]. The positioning of the 2'OH in the C2'-endo nucleotides allow for a hydrogen bond interaction with the PO across the junction that could stabilize the crossover, reminiscent of the 4-way junction in the hairpin ribozyme[45]. Only two of the remaining 23 crossovers nucleotides in 5HT-A fall into the A-form 1a rotamer classification and the majority of the rest are outliers. This indicates that the geometry around this four-way junction samples a unique area of torsional space not yet represented by natural RNA structures in the databases.

6-helix bundle folds through a kinetic trap

The cryo-EM reconstruction of the 6HB RNA (**Fig. 3a**) agrees well with our predicted model (Fig. 1h) with average φ angles of 127 ° (Extended Data Fig. 5b). To stabilize the 6HB, a second design was made by adding one crossover between H1 and H6 at the expense of one crossover between H5 and H6, resulting in H6 functioning as a clasp (6HBC, Supplementary Table 6). The cryo-EM

reconstruction of 6HBC shows that H6 has a θ angle of 45 °, forming a bridge over the 5 other parallel helices (**Fig. 3b**). When using a variant of 6HBC, with the same topology, for protein binding studies (6HBC-PBS, Supplementary Table 7), we observed that after extended periods of time at room temperature, the structure has matured into a second conformation in which H6 is now more parallel to the adjacent helices (**Fig. 3c**). To verify that this observation was not just a consequence of the protein binding motifs, we froze the original 6HBC sample at an intermediary time point (5 hours post transcription) and observed that cryo-EM images contain both conformations, from which we were able to reconstruct both conformers from a single data set (Extended Data Fig. 1) and analyze 3D variability (Supplementary Video 3).

To better understand the transition, we followed the maturation of the 6HBC by SAXS, taking 15-minute data collection windows for 17.5 hours (**Fig. 3d**). The SAXS data only vary in intermediate to high q, which is expected for an internal structural rearrangement. Only subtle rigid body movements from our cryo-EM based models were needed to optimize the χ^2 of the fit from 9.99 and 6.12 to 2.15 ± 0.2 and 1.92 ± 0.1 for the young and mature conformers, respectively (**Fig. 3e**). The intensity at q = 0.09 $Å^{-1}$ was plotted as a function of time (**Fig. 3f**) and shows that the transition takes place from 6 to 8 hours with a clear plateau on either side. The intermediate scattering curves can be described well by a linear combination of the scattering from the starting and end conformers, indicating a two-stage transition (**Fig. 3g**).

The mechanism for the slow transition was suggested by superposition of the models of the two 6HBC conformers, which revealed that the AA base stack in the KL of H6 changes position from being oriented towards the interior of the bundle to the exterior (Extended Data Fig. 8b). For the transformation to occur, each half of the clasp helix must rotate 180° in opposite directions, which necessitates the transient breaking of the KL tertiary interactions (Supplementary Video 4). As well as these major rotations, there are also substantial changes to the φ angles of helices 3, 4 and 5 at the 3' end of the bundle, and more subtle changes at the 5' end of the bundle that are necessary to accommodate the final position of the clasp helix (Extended Data Fig. 4c,d). The φ, θ and seam twist angles observed in the mature structure are closer to those observed in the 6HB without the clasp, hinting that the optimization of these angles could be a driving force for structural transformation.

16-helix satellites by tomography

The 6HBC was extended with "wings" by adding bKLs with shortened versions of the 5HT-B to form a "satellite" shape (16HS, Supplementary Table 8). The resulting 16HS is composed of three

independent folding domains demonstrating that RNA origami of higher complexity can be produced by cotranscriptional folding. The bKL has so far been studied in constrained conformations and here we capture its solution structure for the first time. NS-TEM single particle analysis yields 2D class averages where the 16HS appears to be flattened by interactions with the surface. In the particle class averages, one end of the 6HBC is opened, possibly stemming from kinetic trapping related to the clasp on the bundle (**Fig. 4a,b** and Extended Data Fig. 9a). Our attempts at using single particle averaging methods on cryo-EM data failed to produce a reconstruction containing the core and both wings (data not shown). To circumvent this problem, we switched to individual particle electron tomography (IPET) methods to reconstruct the satellite from individual molecules without averaging. We were able to reconstruct 12 individual particles from our data (**Fig. 4c** and Extended Data Fig. 10). Flexible fitting of models (**Fig. 4d**) showed the structure has variation in bKL angles in a range of ~150 ° and in the rotation of the 5HT component with respect to the core 6HBC.

Discussion

In this study we have gained insight on the native hydrated structure of RNA origami to reveal structural motifs, design parameters and cotranscriptional folding, which will greatly facilitate future design efforts. The main factor limiting the resolution of our cryo-EM reconstructions appears to be a continuous dynamic motion that is inherent to most RNA structures. We identified the crossovers and helical termini as the main points of flexibility, which can be used to design more rigid structures by the adoption of shorter crossover distances and/or the addition of stabilizing motifs. The flexibility of helical termini is of particular concern since it will affect the precision by which we can use RNA origami to place molecular elements such as aptamers for proteins or small molecules[4]. In contrast to the numerous backbone probing methods that has been used to study the folding of RNA[46,47], our solution-structure characterization reveal conformations and dynamics that would not be identifiable by other methods.

Our previous structural assumptions about RNA origami were challenged by the high-resolution cryo-EM data: The first assumption, that a DX containing an integer number of full-turns between crossovers will force the helices to be perfectly parallel, turns out to be incorrect. We found that crossovers constitute a new structural motif involving the 2'OH of one of the junction positions, with a preferred angle of roughly 11.3° ± 7.3°. The second assumption, that a KL corresponds to 9 bps of A-form helix and is a rigid 180° block irrespective of the KL sequence, turns out to be mostly valid. KLs in all of the models appear to share a similar conformation

irrespective of sequence, but the motif corresponds more closely to 8 bps. A third assumption, that the number of bps between two crossovers connecting three adjacent helices dictates the angle φ between adjacent helices, appears to also be true, but only when the torsion in the structure is reduced as in the twist-corrected 5HT-A-TC. In addition to these revisions to the core assumptions of RNA origami design, we have also discovered new dynamic properties of RNA origami nanostructures and their folding.

Serendipitously, we identified a kinetic folding trap of the 6HBC that slowly matures into a more thermodynamically favorable state. We suggest that the kinetic trap forms during the cotranscriptional folding process where the KL partners from H6 first meet when their respective crossovers are at their relaxed angle (~45 °) and thus topologically blocks the bundle from further compacting. The slow transition is likely caused by the strong H6 KL interaction, which is only gradually overcome by a series of progressively more stable microstates that take multiple hours to traverse before the KL breaks to allow the structure to mature further. Both the changes observed in the SAXS data and our cryo-EM models suggest that the structure matures through decrease in solvent-accessible surface area by helix packing and freeing of caged water molecules and/or the sharing of cations (K^+ or Mg^{2+}). Kinetic traps are known to form as a result of the early formation of pseudoknots that blocks later base pairs from forming, and can be prevented by delaying the formation of the pseudoknot[48]. Our mechanism suggests that, either by weakening the KL, or by introducing a transient antisense oligo that binds to the H6 KL to function as a chaperone, may avoid the misfolded conformation. The observed trap is reminicent to traps in ribosomal folding that requires chaperones for remodelling late assembly intermediates[47].

Finally, cryo-ET allowed the characterization of RNA origami at the single molecule level, which revealed global conformational dynamics of branched domains in the “satellite” structure. It has recently been shown that DNA origami “sign-posts” can be used as extracellular tags for cryo-ET[49]. Similarly, RNA origamis “satellites” may serve as genetically expressible tags for cryo-ET to facilitate exploration and reporting from intracellular space. RNA origami can serve as a platform for combining fluorescent RNA aptamers[50], dynamic RNA switches[51] and RNA strand displacement[52], which can enable the next generation of advanced RNA control elements for synthetic biology. RNA nanostructures also has a bright future in RNA therapeutics, because of their low immunogenicity, tunable immunostimulatory properties, and programmability[53]. One of the current issues is that the RNA particles are hierarchically assembled with multiple intermediate purification steps, resulting low yield[5]. However, by using cotranscriptional folding to produce

RNA particles we can take advantage of the high fidelity of coupled synthesis and self-assembly to enable large-scale production of RNA medicine.

References

1 Cruz, J. A. & Westhof, E. The dynamic landscapes of RNA architecture. *Cell* **136**, 604-609, doi:10.1016/j.cell.2009.02.003 (2009).

2 Rodgers, M. L. & Woodson, S. A. A roadmap for rRNA folding and assembly during transcription. *Trends Biochem Sci* **46**, 889-901, doi:10.1016/j.tibs.2021.05.009 (2021).

3 Geary, C., Rothemund, P. W. & Andersen, E. S. A single-stranded architecture for cotranscriptional folding of RNA nanostructures. *Science* **345**, 799-804, doi:10.1126/science.1253920 (2014).

4 Geary, C., Grossi, G., McRae, E. K. S., Rothemund, P. W. K. & Andersen, E. S. RNA origami design tools enable cotranscriptional folding of kilobase-sized nanoscaffolds. *Nat Chem*, doi:10.1038/s41557-021-00679-1 (2021).

5 Chandler, M., Panigaj, M., Rolband, L. A. & Afonin, K. A. Challenges to optimizing RNA nanostructures for large scale production and controlled therapeutic properties. *Nanomedicine (Lond)*, doi:10.2217/nnm-2020-0034 (2020).

6 Li, M. *et al.* In vivo production of RNA nanostructures via programmed folding of single-stranded RNAs. *Nat Commun* **9**, 2196, doi:10.1038/s41467-018-04652-4 (2018).

7 Liu, D. *et al.* Branched kissing loops for the construction of diverse RNA homooligomeric nanostructures. *Nat Chem* **12**, 249-259, doi:10.1038/s41557-019-0406-7 (2020).

8 Jepsen, M. D. E. *et al.* Development of a genetically encodable FRET system using fluorescent RNA aptamers. *Nat Commun* **9**, 18, doi:10.1038/s41467-017-02435-x (2018).

9 Jasinski, D., Haque, F., Binzel, D. W. & Guo, P. Advancement of the Emerging Field of RNA Nanotechnology. *ACS Nano* **11**, 1142-1164 (2017).

10 Ohno, H., Akamine, S. & Saito, H. RNA nanostructures and scaffolds for biotechnology applications. *Curr Opin Biotechnol* **58**, 53-61, doi:10.1016/j.copbio.2018.11.006 (2019).

11 Kim, J. & Franco, E. RNA nanotechnology in synthetic biology. *Curr Opin Biotechnol* **63**, 135-141, doi:10.1016/j.copbio.2019.12.016 (2020).

12 Seeman, N. C. Nucleic-Acid Junctions and Lattices. *J. Theor. Biol.* **99**, 237-247, doi:10.1016/0022-5193(82)90002-9 (1982).

13 Winfree, E., Liu, F., Wenzler, L. A. & Seeman, N. C. Design and self-assembly of two-dimensional DNA crystals. *Nature* **394**, 539-544, doi:10.1038/28998 (1998).

14 Chen, J. H. & Seeman, N. C. Synthesis from DNA of a molecule with the connectivity of a cube. *Nature* **350**, 631-633, doi:10.1038/350631a0 (1991).

15 Wang, H., Di Gate, R. J. & Seeman, N. C. An RNA topoisomerase. *Proc Natl Acad Sci U S A* **93**, 9477-9482, doi:10.1073/pnas.93.18.9477 (1996).

16 Weizmann, Y. & Andersen, E. S. RNA nanotechnology—The knots and folds of RNA nanoparticle engineering. *MRS Bulletin* **42**, 930-935, doi:10.1557/mrs.2017.277 (2017).

17 Rothemund, P. W. K. Folding DNA to create nanoscale shapes and patterns. *Nature* **440**, 297-302, doi:10.1038/nature04586 (2006).

18 Torring, T., Voigt, N. V., Nangreave, J., Yan, H. & Gothelf, K. V. DNA origami: a quantum leap for self-assembly of complex structures. *Chem Soc Rev* **40**, 5636-5646, doi:10.1039/c1cs15057j (2011).

19 Severcan, I. *et al.* A polyhedron made of tRNAs. *Nat. Chem.* **2**, 772-772 (2010).

20 Afonin, K. A. *et al.* In vitro Assembly of Cubic RNA-Based Scaffolds Designed in silico. *Nat. Nanotechnol.* **5**, 676-682, doi:10.1038/nnano.2010.160 (2010).
21 Zakrevsky, P. *et al.* Truncated tetrahedral RNA nanostructures exhibit enhanced features for delivery of RNAi substrates. *Nanoscale* **12**, 2555-2568, doi:10.1039/c9nr08197f (2020).
22 Xu, C. *et al.* 3D RNA nanocage for encapsulation and shielding of hydrophobic biomolecules to improve the in vivo biodistribution. *Nano Res* **13**, 3241-3247, doi:10.1007/s12274-020-2996-1 (2020).
23 Ko, S. H. *et al.* Synergistic self-assembly of RNA and DNA molecules. *Nat Chem* **2**, 1050-1055, doi:10.1038/nchem.890 (2010).
24 Hao, C. *et al.* Construction of RNA nanocages by re-engineering the packaging RNA of Phi29 bacteriophage. *Nat Commun* **5**, 3890, doi:10.1038/ncomms4890 (2014).
25 Afonin, K. A. *et al.* Multifunctional RNA nanoparticles. *Nano Lett* **14**, 5662-5671, doi:10.1021/nl502385k (2014).
26 Yu, J., Liu, Z., Jiang, W., Wang, G. & Mao, C. De novo design of an RNA tile that self-assembles into a homo-octameric nanoprism. *Nat Commun* **6**, 5724, doi:10.1038/ncomms6724 (2015).
27 Geary, C., Chworos, A., Verzemnieks, E., Voss, N. R. & Jaeger, L. Composing RNA Nanostructures from a Syntax of RNA Structural Modules. *Nano Lett* **17**, 7095-7101, doi:10.1021/acs.nanolett.7b03842 (2017).
28 Kappel, K. *et al.* Accelerated cryo-EM-guided determination of three-dimensional RNA-only structures. *Nat Methods* **17**, 699-707, doi:10.1038/s41592-020-0878-9 (2020).
29 Kappel, K. *et al.* De novo computational RNA modeling into cryo-EM maps of large ribonucleoprotein complexes. *Nat Methods* **15**, 947-954, doi:10.1038/s41592-018-0172-2 (2018).
30 Zhang, K. *et al.* Cryo-EM structure of a 40 kDa SAM-IV riboswitch RNA at 3.7 A resolution. *Nat Commun* **10**, 5511, doi:10.1038/s41467-019-13494-7 (2019).
31 Zhang, K. *et al.* Cryo-EM and antisense targeting of the 28-kDa frameshift stimulation element from the SARS-CoV-2 RNA genome. *Nat Struct Mol Biol* **28**, 747-754, doi:10.1038/s41594-021-00653-y (2021).
32 Su, Z. *et al.* Cryo-EM structures of full-length Tetrahymena ribozyme at 3.1 A resolution. *Nature* **596**, 603-607, doi:10.1038/s41586-021-03803-w (2021).
33 Andersen, E. S. *et al.* Self-assembly of a nanoscale DNA box with a controllable lid. *Nature* **459**, 73-U75, doi:10.1038/nature07971 (2009).
34 Bai, X. C., Martin, T. G., Scheres, S. H. & Dietz, H. Cryo-EM structure of a 3D DNA-origami object. *Proc Natl Acad Sci U S A* **109**, 20012-20017, doi:10.1073/pnas.1215713109 (2012).
35 Martin, T. G. *et al.* Design of a molecular support for cryo-EM structure determination. *Proc Natl Acad Sci U S A* **113**, E7456-E7463, doi:10.1073/pnas.1612720113 (2016).
36 Laing, C. & Schlick, T. Analysis of four-way junctions in RNA structures. *J Mol Biol* **390**, 547-559, doi:10.1016/j.jmb.2009.04.084 (2009).
37 Ennifar, E. *et al.* The crystal structure of the dimerization initiation site of genomic HIV-1 RNA reveals an extended duplex with two adenine bulges. *Structure* **7**, 1439-1449, doi:10.1016/s0969-2126(00)80033-7 (1999).
38 Ennifar, E., Walter, P., Ehresmann, B., Ehresmann, C. & Dumas, P. Crystal structures of coaxially stacked kissing complexes of the HIV-1 RNA dimerization initiation site. *Nat. Struct. Biol.* **8**, 1064-1064 (2001).

39 Ennifar, E. & Dumas, P. Polymorphism of bulged-out residues in HIV-1 RNA DIS kissing complex and structure comparison with solution studies. *J Mol Biol* **356**, 771-782, doi:10.1016/j.jmb.2005.12.022 (2006).

40 Kieken, F., Paquet, F., Brule, F., Paoletti, J. & Lancelot, G. A new NMR solution structure of the SL1 HIV-1Lai loop-loop dimer. *Nucleic Acids Res* **34**, 343-352, doi:10.1093/nar/gkj427 (2006).

41 Baba, S. *et al.* Solution RNA structures of the HIV-1 dimerization initiation site in the kissing-loop and extended-duplex dimers. *J Biochem* **138**, 583-592, doi:10.1093/jb/mvi158 (2005).

42 Takahashi, K. *et al.* NMR analysis of intra- and inter-molecular stems in the dimerization initiation site of the HIV-1 genome. *J Biochem* **127**, 681-686, doi:10.1093/oxfordjournals.jbchem.a022657 (2000).

43 Liu, D., Shao, Y., Piccirilli, J. A. & Weizmann, Y. Structures of artificially designed discrete RNA nanoarchitectures at near-atomic resolution. *Sci Adv* **7**, eabf4459, doi:10.1126/sciadv.abf4459 (2021).

44 Richardson, J. S. *et al.* RNA backbone: consensus all-angle conformers and modular string nomenclature (an RNA Ontology Consortium contribution). *RNA* **14**, 465-481, doi:10.1261/rna.657708 (2008).

45 Rupert, P. B., Massey, A. P., Sigurdsson, S. T. & Ferre-D'Amare, A. R. Transition state stabilization by a catalytic RNA. *Science* **298**, 1421-1424, doi:10.1126/science.1076093 (2002).

46 Watters, K. E., Strobel, E. J., Yu, A. M., Lis, J. T. & Lucks, J. B. Cotranscriptional folding of a riboswitch at nucleotide resolution. *Nat Struct Mol Biol* **23**, 1124-1131, doi:10.1038/nsmb.3316 (2016).

47 Clatterbuck Soper, S. F., Dator, R. P., Limbach, P. A. & Woodson, S. A. In vivo X-ray footprinting of pre-30S ribosomes reveals chaperone-dependent remodeling of late assembly intermediates. *Mol Cell* **52**, 506-516, doi:10.1016/j.molcel.2013.09.020 (2013).

48 Isambert, H. The jerky and knotty dynamics of RNA. *Methods* **49**, 189-196, doi:10.1016/j.ymeth.2009.06.005 (2009).

49 Silvester, E. *et al.* DNA origami signposts for identifying proteins on cell membranes by electron cryotomography. *Cell* **184**, 1110-1121 e1116, doi:10.1016/j.cell.2021.01.033 (2021).

50 Zhou, H. & Zhang, S. Recent Development of Fluorescent Light-Up RNA Aptamers. *Crit Rev Anal Chem*, 1-18, doi:10.1080/10408347.2021.1907735 (2021).

51 Shibata, T. *et al.* Protein-driven RNA nanostructured devices that function in vitro and control mammalian cell fate. *Nat. Commun.* **8**, 540, doi:10.1038/s41467-017-00459-x (2017).

52 Liu, H. *et al.* Kinetics of RNA and RNA:DNA Hybrid Strand Displacement. *ACS Synth Biol* **10**, 3066-3073, doi:10.1021/acssynbio.1c00336 (2021).

53 Guo, S. *et al.* Tuning the size, shape and structure of RNA nanoparticles for favorable cancer targeting and immunostimulation. *Wiley Interdiscip Rev Nanomed Nanobiotechnol* **12**, e1582, doi:10.1002/wnan.1582 (2020).

54 Lorenz, R. *et al.* ViennaRNA Package 2.0. *Algorithms Mol. Biol.* **6**, 26, doi:10.1186/1748-7188-6-26 (2011).

55 Zadeh, J. N. *et al.* NUPACK: Analysis and design of nucleic acid systems. *J. Comput. Chem.* **32**, 170-173, doi:10.1002/jcc.21596 (2011).

56 Mastronarde, D. N. Automated electron microscope tomography using robust prediction of specimen movements. *J Struct Biol* **152**, 36-51, doi:10.1016/j.jsb.2005.07.007 (2005).

57 Punjani, A., Rubinstein, J. L., Fleet, D. J. & Brubaker, M. A. cryoSPARC: algorithms for rapid unsupervised cryo-EM structure determination. *Nat. Methods* **14**, 290-296, doi:10.1038/nmeth.4169 (2017).
58 Tegunov, D. & Cramer, P. Real-time cryo-electron microscopy data preprocessing with Warp. *Nat Methods* **16**, 1146-1152, doi:10.1038/s41592-019-0580-y (2019).
59 Punjani, A., Zhang, H. & Fleet, D. J. Non-uniform refinement: adaptive regularization improves single-particle cryo-EM reconstruction. *Nat Methods* **17**, 1214-1221, doi:10.1038/s41592-020-00990-8 (2020).
60 Punjani, A. & Fleet, D. J. 3D variability analysis: Resolving continuous flexibility and discrete heterogeneity from single particle cryo-EM. *J Struct Biol* **213**, 107702, doi:10.1016/j.jsb.2021.107702 (2021).
61 Zheng, S. Q. *et al.* MotionCor2: anisotropic correction of beam-induced motion for improved cryo-electron microscopy. *Nat Methods* **14**, 331-332, doi:10.1038/nmeth.4193 (2017).
62 Kremer, J. R., Mastronarde, D. N. & McIntosh, J. R. Computer visualization of three-dimensional image data using IMOD. *J Struct Biol* **116**, 71-76, doi:10.1006/jsbi.1996.0013 (1996).
63 Zhang, K. Gctf: Real-time CTF determination and correction. *J Struct Biol* **193**, 1-12, doi:10.1016/j.jsb.2015.11.003 (2016).
64 Fernandez, J. J., Li, S. & Crowther, R. A. CTF determination and correction in electron cryotomography. *Ultramicroscopy* **106**, 587-596, doi:10.1016/j.ultramic.2006.02.004 (2006).
65 Wu, H. *et al.* An Algorithm for Enhancing the Image Contrast of Electron Tomography. *Sci Rep* **8**, 16711, doi:10.1038/s41598-018-34652-9 (2018).
66 Zhang, L. & Ren, G. IPET and FETR: experimental approach for studying molecular structure dynamics by cryo-electron tomography of a single-molecule structure. *PLoS One* **7**, e30249, doi:10.1371/journal.pone.0030249 (2012).
67 Zhai, X. *et al.* LoTToR: An Algorithm for Missing-Wedge Correction of the Low-Tilt Tomographic 3D Reconstruction of a Single-Molecule Structure. *Sci Rep* **10**, 10489, doi:10.1038/s41598-020-66793-1 (2020).
68 Ludtke, S. J., Baldwin, P. R. & Chiu, W. EMAN: semiautomated software for high-resolution single-particle reconstructions. *J Struct Biol* **128**, 82-97, doi:10.1006/jsbi.1999.4174 (1999).
69 Pettersen, E. F. *et al.* UCSF Chimera--a visualization system for exploratory research and analysis. *J Comput Chem* **25**, 1605-1612, doi:10.1002/jcc.20084 (2004).
70 Goddard, T. D. *et al.* UCSF ChimeraX: Meeting modern challenges in visualization and analysis. *Protein Sci* **27**, 14-25, doi:10.1002/pro.3235 (2018).
71 Pettersen, E. F. *et al.* UCSF ChimeraX: Structure visualization for researchers, educators, and developers. *Protein Sci* **30**, 70-82, doi:10.1002/pro.3943 (2021).
72 Croll, T. I. ISOLDE: a physically realistic environment for model building into low-resolution electron-density maps. *Acta Crystallogr D Struct Biol* **74**, 519-530, doi:10.1107/S2059798318002425 (2018).
73 Rodrigues, J., Teixeira, J. M. C., Trellet, M. & Bonvin, A. pdb-tools: a swiss army knife for molecular structures. *F1000Res* **7**, 1961, doi:10.12688/f1000research.17456.1 (2018).
74 Liebschner, D. *et al.* Macromolecular structure determination using X-rays, neutrons and electrons: recent developments in Phenix. *Acta Crystallogr D Struct Biol* **75**, 861-877, doi:10.1107/S2059798319011471 (2019).

75 Terwilliger, T. C. *et al.* Model morphing and sequence assignment after molecular replacement. *Acta Crystallogr D Biol Crystallogr* **69**, 2244-2250, doi:10.1107/S0907444913017770 (2013).
76 Afonine, P. V. *et al.* New tools for the analysis and validation of cryo-EM maps and atomic models. *Acta Crystallogr D Struct Biol* **74**, 814-840, doi:10.1107/S2059798318009324 (2018).
77 Williams, C. J. *et al.* MolProbity: More and better reference data for improved all-atom structure validation. *Protein Sci* **27**, 293-315, doi:10.1002/pro.3330 (2018).
78 Richardson, J. S., Williams, C. J., Videau, L. L., Chen, V. B. & Richardson, D. C. Assessment of detailed conformations suggests strategies for improving cryoEM models: Helix at lower resolution, ensembles, pre-refinement fixups, and validation at multi-residue length scale. *J Struct Biol* **204**, 301-312, doi:10.1016/j.jsb.2018.08.007 (2018).
79 Zok, T., Popenda, M. & Szachniuk, M. MCQ4Structures to compute similarity of molecule structures. *Central European Journal of Operations Research* **22**, 457-473, doi:10.1007/s10100-013-0296-5 (2014).
80 Meier, M. *et al.* Structure and hydrodynamics of a DNA G-quadruplex with a cytosine bulge. *Nucleic Acids Res* **46**, 5319-5331, doi:10.1093/nar/gky307 (2018).
81 Lavery, R., Moakher, M., Maddocks, J. H., Petkeviciute, D. & Zakrzewska, K. Conformational analysis of nucleic acids revisited: Curves+. *Nucleic Acids Res* **37**, 5917-5929, doi:10.1093/nar/gkp608 (2009).
82 Blanchet, C., Pasi, M., Zakrzewska, K. & Lavery, R. CURVES+ web server for analyzing and visualizing the helical, backbone and groove parameters of nucleic acid structures. *Nucleic Acids Res* **39**, W68-73, doi:10.1093/nar/gkr316 (2011).
83 Lyngso, J. & Pedersen, J. S. A high-flux automated laboratory small-angle X-ray scattering instrument optimized for solution scattering. *Journal of Applied Crystallography* **54**, 295-305, doi:doi:10.1107/S1600576720016209 (2021).
84 Li, Y., Beck, R., Huang, T., Choi, M. C. & Divinagracia, M. Scatterless hybrid metal-single-crystal slit for small-angle X-ray scattering and high-resolution X-ray diffraction. *Journal of Applied Crystallography* **41**, 1134-1139, doi:doi:10.1107/S0021889808031129 (2008).
85 Steiner, E. M. *et al.* The structure of the N-terminal module of the cell wall hydrolase RipA and its role in regulating catalytic activity. *Proteins* **86**, 912-923, doi:10.1002/prot.25523 (2018).
86 Carragher, B. *et al.* Leginon: an automated system for acquisition of images from vitreous ice specimens. *J Struct Biol* **132**, 33-45, doi:10.1006/jsbi.2000.4314 (2000).
87 Tang, G. *et al.* EMAN2: an extensible image processing suite for electron microscopy. *J. Struct. Biol.* **157**, 38-46, doi:10.1016/j.jsb.2006.05.009 (2007).
88 Rames, M., Yu, Y. & Ren, G. Optimized negative staining: a high-throughput protocol for examining small and asymmetric protein structure by electron microscopy. *J Vis Exp*, e51087, doi:10.3791/51087 (2014).
89 Zhang, L. *et al.* An optimized negative-staining protocol of electron microscopy for apoE4 POPC lipoprotein. *J Lipid Res* **51**, 1228-1236, doi:10.1194/jlr.D002493 (2010).

Acknowledgments:

We acknowledge the EMBION Cryo-EM Facility at iNANO, Aarhus University, for time under application ID 0042. We would like to thank Poul Nissen and Ariane Briegel for their early support of the project and valuable discussion, Steffen Sparvath for early design and experiments with the 6-helix bundle, and Ariane Briegel and Hans Christian Høiberg for early negative stain TEM characterization of 6-helix bundles. Thanks to Rita Rosendahl and Claus Bus for technical assistance.

Funding:

The work at iNANO was supported by the Independent Research Fund Denmark under the Research Project 1 grant (9040-00425B). E.K.S.M was also partially supported by the Canadian Natural Sciences and Engineering Research Council by a post-doctoral fellowship (532417). Computational resources for the project were in part supported by the Carlsberg Foundation Research Infrastructure grant (CF20-0635). E.S.A. acknowledges support by an European Research Council (ERC) Consolidator grant (683305) and Novo Nordisk Foundation Ascending Investigator grant (0060694). The work at the molecular foundry, LBNL was supported by the Office of Science, Office of Basic Energy Sciences of the United States Department of Energy (contract no. DE-AC02-05CH11231), and J.L. and G.R were partially supported by grants from the US National Institutes of Health (no. R01HL115153, R01 GM104427, R01MH077303, and R01DK042667).

Author contributions:

Conceptualization: EKSM, NSP, MN, CG, ESA
Methodology: EKSM, MN, HØR, NSP, CG
Data Curation: EKSM, AB, HØR
Investigation: EKSM, HØR, AB, THB, ESA
Visualization: EKSM, ESA
Funding acquisition: EKSM, JSP, GR, ESA
Project administration: JSP, CG, ESA
Supervision: JSP, CG, GR, ESA
Writing – original draft: EKSM
Writing – review & editing: EKSM, HØR, MN, NSP, AB, THB, JSP, CG, ESA

Competing interests: Authors declare that they have no competing interests.

Data and materials availability:

The sequences of the designs used, and images of the blueprints are available in the Suplementary Materials. The corresponding author will gladly provide text versions of the blueprints upon request. The volumes from the final refinements of our cryo-EM SPA datasets have been deposited to the ePDB under accession codes EMD-13633, EMD-13926, EMD-13636, EMD-13592, EMD-13627, EMD-13628, EMD-13630, EMD-13626, EMD-13625, for 5HT-A, 5HT-A-twist-corrected, 5HT-B, 5HT-B-3X, 6HB, 6HBC-young-1, 6HBC-PBS-mature-1, 6HBC-young2, 6HBC-mature-2, respectively, and the atomic models under the PDB codes 7PTQ, 7QDU, 7PTS, 7PTK, 7PTL for 5HT-A, 5HT-A-twist-corrected, 5HT-B, 6HBC-young-1 and 6HBC-mature-1, respectively. The volumes from the reconstructed IPET data of the 16-helix satellite have been deposited to the ePDB under the accession codes EMD-25078 and EMDB-25080-25090.

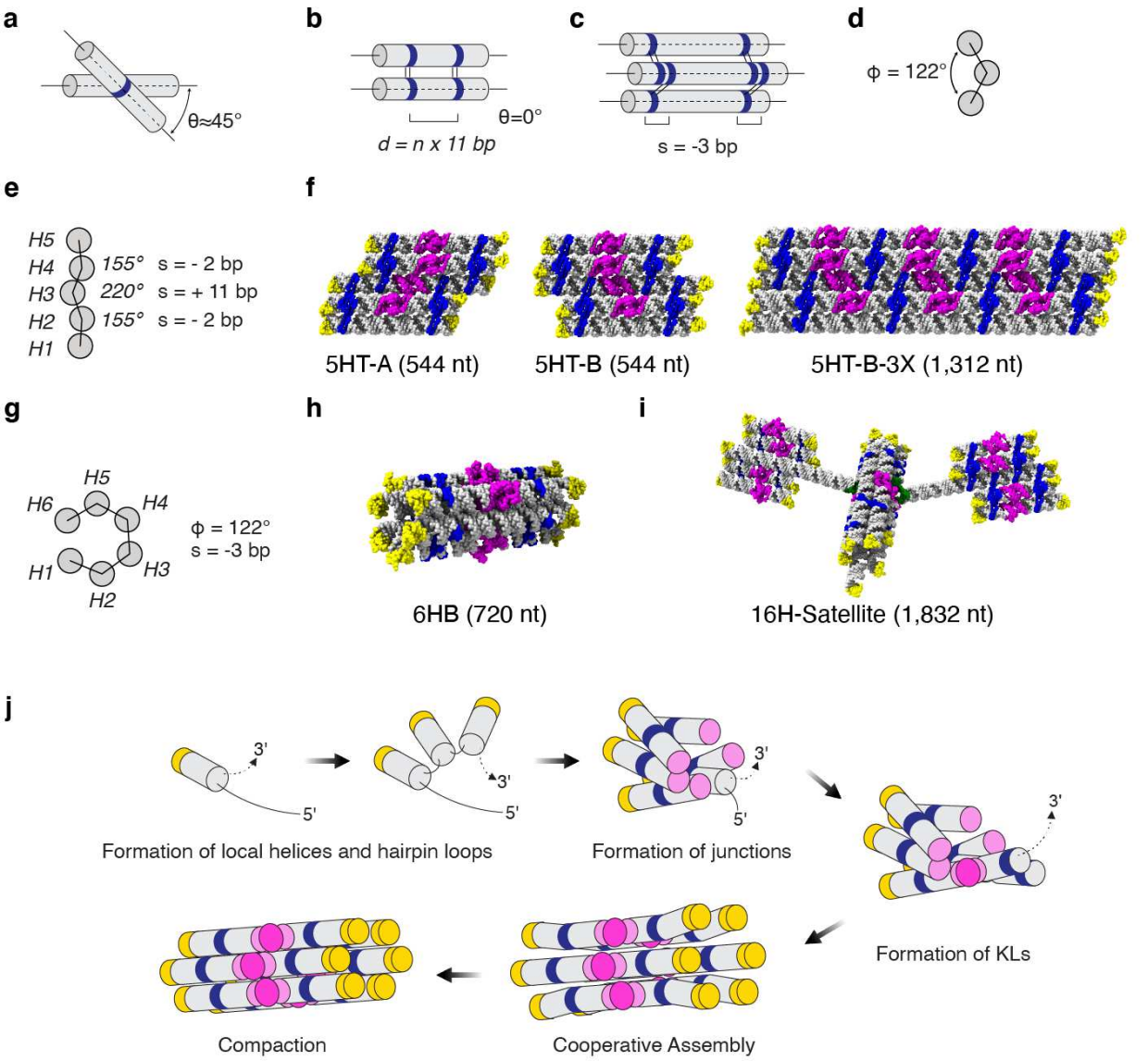

Fig. 1. Principles for RNA origami folding and design. a, Depiction of the relaxed θ angle observed in natural antiparallel crossovers. **b**, DX with strained 0 ° θ angle used in RNA origami designs, where *d* refers to DX spacing in bp and *n* to the number of turns. **c**, Depiction of a -3-bp DT seam and its effect on **d** the φ angle. **e**, Predicted φ angles for a designed 5HT building block and **f** molecular models of three designs. **g**, Predicted φ angles for **h**, a 6HB and **i** a 16HS multi-domain structure. Tetraloops are depicted in yellow, crossovers in blue, KLs in magenta, and bKLs in green in molecular models. **j**, Hypothetical cotranscriptional folding and maturation by compaction of a 6HB RNA origami. A-form helix shown as grey cylinders, tetraloops as yellow caps, junctions as blue rings, and kissing loops as purple circles.

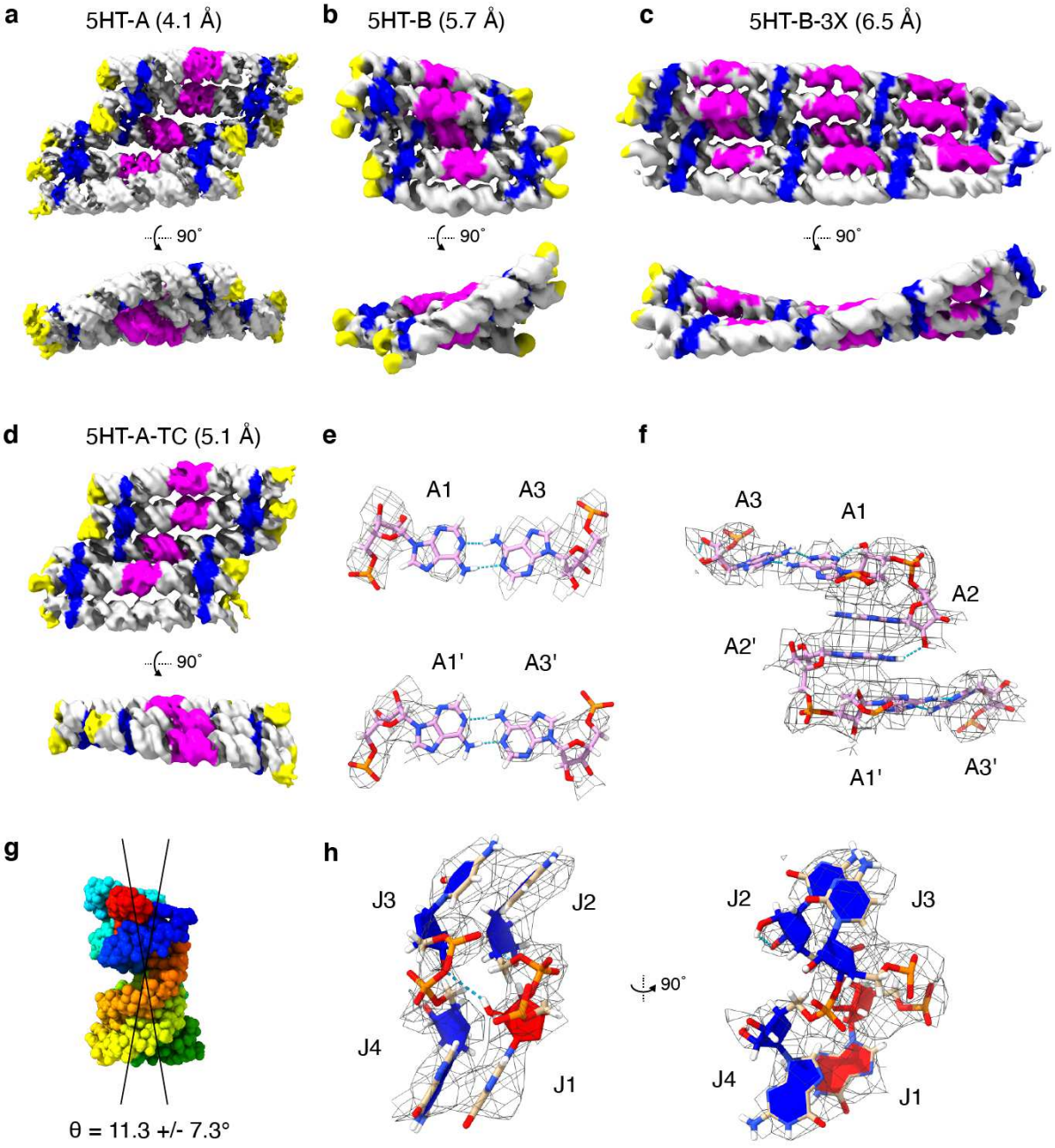

Fig. 2. Cryo-EM characterization of 5-helix tile structures. a-d, Cryo-EM reconstructions for the 5HT designs with resolution indicated in brackets. Coloring has been applied to the maps through the motifs modeled into the map. Tetraloops are depicted in yellow, crossovers in blue and KLs in magenta. The relative scale of the reconstructions can be estimated by the thickness of a helix, which is ~2 nm. **e**, Trans WC-WC interactions of A1 and A3 from H3 KL. **f**, Base stacking of A2 and A2' and 2'O to NH_2 hydrogen bonds from the H3 KL. **g**, Depiction of the most common θ angle for the interior crossovers of 5HT-A. Color show strand direction from 5' (blue) to 3' (red). **h**, Views of the crossover junctions from 5HT-A. C3'-endo nucleotides are colored blue, C2'-endo nucleotides are colored red, cross-strand hydrogen bond (cyan) between the C2'-endo OH and a PO. J refer to junction nucleotides and are numbered from 5' to 3'.

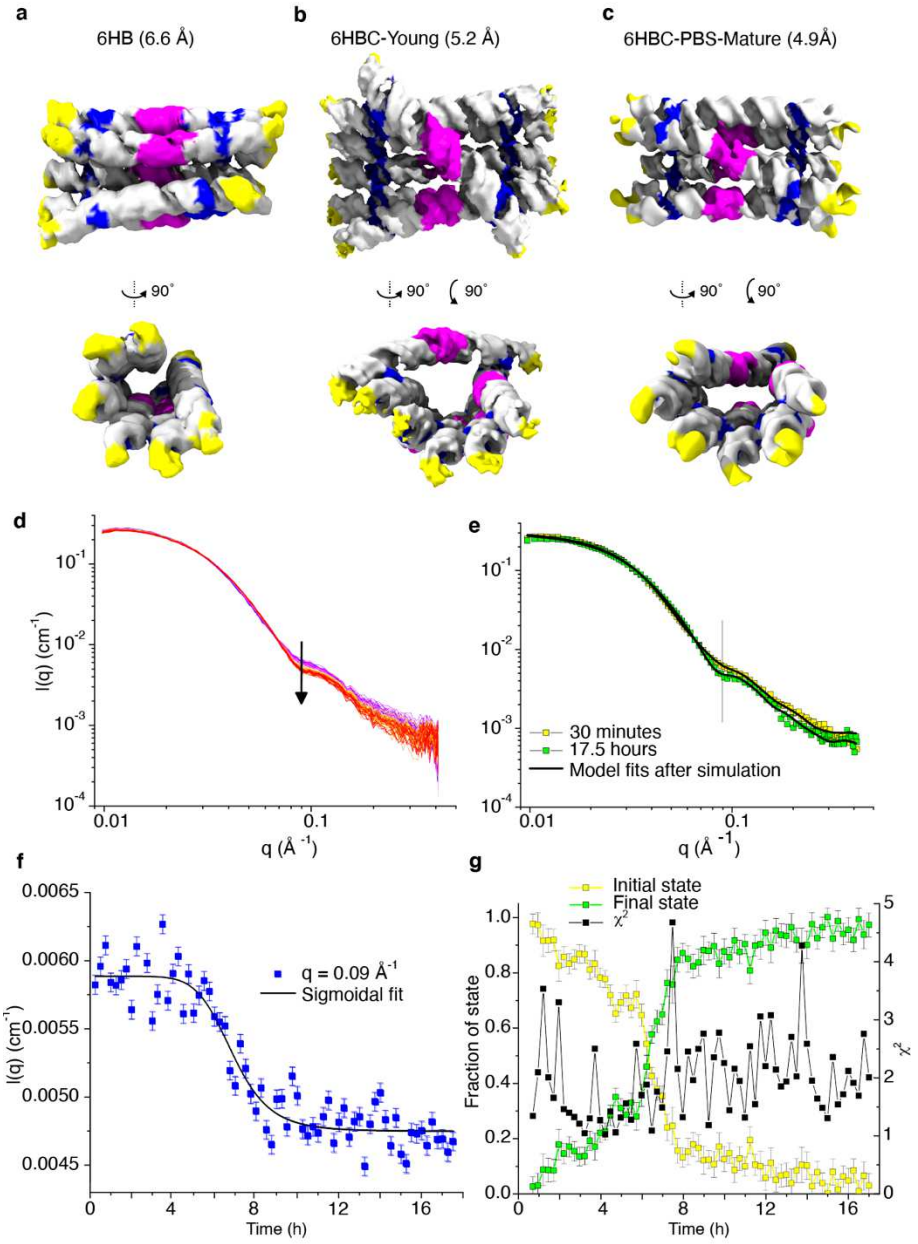

Fig. 3. Cryo-EM and SAXS characterization of 6-helix bundle structures. Cryo-EM single-particle averaging reconstructions of the 6HB **a**, 6HBC **b**, and 6HBC-PBS **c** with resolution indicated in brackets. Coloring has been applied to the maps through the motifs modeled into the map, tetraloops are depicted in yellow, crossovers in blue and KLs in magenta. In the case of panel c, tetraloops were modelled into the density where protein binding domains should be based on our design. **d**, SAXS measurements on the 6HBC structure, showing change in scattering over time as the structure matures (black arrow shows the direction of change with time). **e**, Fit of the predicted scattering from rigid-body optimized 6HBC-Young and 6HBC-Mature models to the experimental scattering from early and late time points. Black line denotes q = 0.09 Å^{-1}. **f**, The intensity at q = 0.09 Å^{-1} is plotted as a function of time and shows that the transition takes place from 6-8 hours. **g**, A linear combination analysis shows that all intermediate data frames can be described as a linear combination of the experimental data for the initial and mature state because χ^2 on average stays constant.

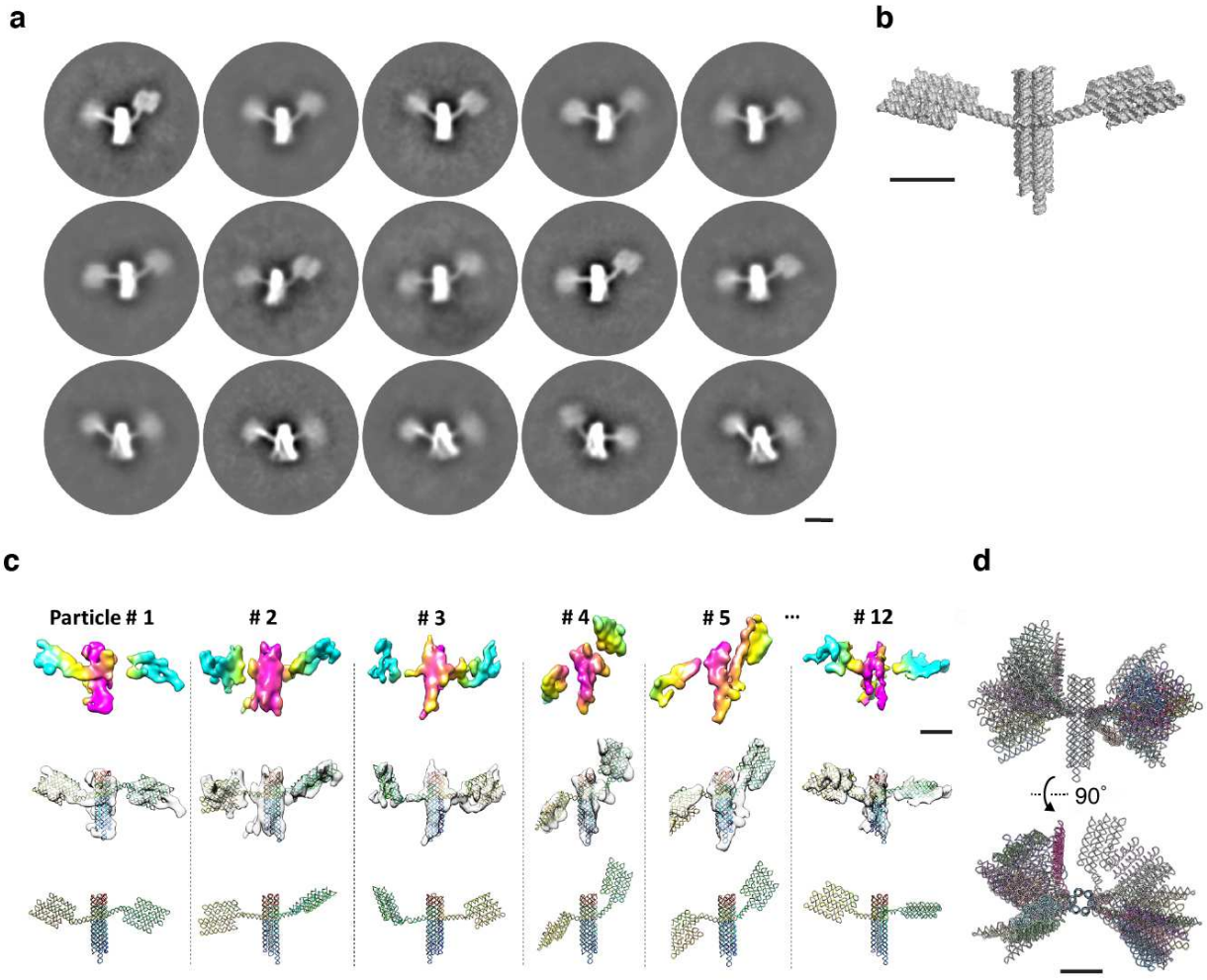

Fig. 4. Structural dynamics of 16-helix satellite structure. a, 2D class averages of particles picked from negative stain TEM micrographs show a wide range of bKL angles. **b**, Molecular model in a similar orientation to the particles observed in class averages. **c**, Six 3D density maps reconstructed from six representative individual particles of the satellite design imaged by cryogenic electron tomography by IPET (top panel) and their flexible docked structural models (bottom panels). **d**, Superimposition of 12 structural models reveal an additional rotation heterogeneity not observed by negative stain TEM. Scale bars are 10 nm.

Methods

Design and production of RNA origami structures

RNA origami blueprints were designed as described previously[4]. Briefly, a 2D blueprint describing the desired base pairing and kissing loop contacts is input into the revolver program from the RNA Origami Automated Design (ROAD) software suite and hundreds of suggested sequences that could fulfill the requirements are found, the sequence with the lowest ensemble diversity[54] is then chosen and checked in NUPACK[55] for potential alternate conformations.

The best candidate sequence is then ordered as double stranded DNA for cloning into a modified pUC vector. Plasmids are then sequenced to ensure no mutations are present. Plasmids for large scale transcriptions are produced in DH5-alpha cells using the MaxiPrep kit from Machery Nagel. Purified plasmid is then restriction digested overnight with BsaI (New England Biolabs) which cleaves the DNA such that the last template nucleotide is the 3' end of our RNA origami. Plasmid is then purified by triple phenol chloroform extraction followed by ethanol precipitation. The linearized plasmid is then resuspended in RNase Free water and diluted to 0.5 mg/mL.

Transcription reactions are setup in a transcription buffer containing 40 mM Tris-Cl pH 8.0 at 37 °C, 1 mM spermidine, 0.001% Triton X-100, 100 mM DTT, 12 mM $MgCl_2$, 8 mM NTP mix and 0.05 mg/mL template DNA. Transcriptions are started upon addition of in-house prepared T7 polymerase and transcription reactions are carried out for 3 hours at 37 °C. Precipitated inorganic pyrophosphate is pelleted by centrifugation at 17000g for 5 minutes at room temperature. The transcription reaction is then loaded onto a Superose 6 column (Cytiva) equilibrated with 25 mM HEPES pH 8.0, 50 mM KCl and 5 mM $MgCl_2$. The major RNA peak is then collected and concentrated in 10 kDa cutoff Amicon spin concentrators to the desired concentration.

Cryo-EM sample preparation

Ideal sample concentrations for cryo-EM of RNA origami were found in the 2.5-3 mg/mL range as determined by A260 measurements on a DeNovix DS-11. Initial difficulties obtaining samples in the holes of carbon film grids were overcome by switching to all gold grids. We used ProtoChips Au-FLAT 1.2/1.3 300 mesh grids for all samples in this study. Grids were glow-discharged for 45 seconds at 15 mA in a Pelco easiGlow immediately prior to sample application. Grids were plunge-frozen using a Leica GP2; the sample application chamber was kept at 100% humidity and 21 °C.

3 microlitres of sample was applied to the grid which was then blotted with a manually calibrated stopping distance onto a double layer of Watman #1 filter paper using a 4 second delay after application, 6 seconds of blot time and 0 seconds of delay after blotting before plunging into liquid ethane at –184 °C. For cryo-ET specimen preparation of RNA origami satellite, an aliquot (4 μl) of sample solution (1.8 mg/ml) was placed on a lacey carbon, 200 mesh copper grid (Cu-200LC, Electron Microscopy Sciences, Hatfield, PA, USA) that was prior glow-discharged for 15 seconds. After 3 seconds of blotting with filter paper from one side, the grids were flash-frozen in liquid ethane at ~90% humidity and 4 °C with a Leica EM GP rapid-plunging device (Leica, Buffalo Grove, IL, USA) before transferred into liquid nitrogen for storage.

Cryo-EM Single Particle Analysis data collection

Except for the 5HT-B and 6HBC-2 datasets, all data was acquired at 300 keV on a Titan Krios G3i (Thermo Fisher Scientific) equipped with a K3 camera (Gatan/Ametek) and energy filter operated in EFTEM mode using a slit width of 20 eV. The 6HBC-2 and 5HT-B datasets were acquired on Titan Krios G1 equipped with Cs corrector, K2 camera (Gatan/Ametek). Data were collected over a defocus range of -0.5 to -2 micrometers with a targeted dose of 60 $e^-/Å^2$. Automated data collection was performed with EPU and the data saved as gain normalized compressed tiff files (K3) or MRC files (K2) with pixel sizes of 0.645 and 0.86 Å/px, respectively.

Cryo-ET tilt series data acquisition of RNA origami satellite

The cryo-EM specimens of RNA origami satellite were imaged by a Titan Krios G2 TEM (ThermoFisher Scientific) with a Gatan energy filter (Gatan, Inc., Pleasanton, CA, USA), operated under 300 keV. Micrographs were acquired on a Gatan K3 direct electron detector operated in super-resolution mode at a nominal magnification of 81 k× (corresponding to 0.94 Å/pixel) with a defocus of ~2 μm. Tilt series were acquired by SerialEM[56] in a tilting range of ±51° in a tilting step of 3° and total dose of 319 $e^-/Å^2$ (at exposure time of 0.5 s per tilt image). The un-tilt images were acquired at exposure time 2.8 s with total dose of 50 $e^-/Å^2$.

Cryo-EM Single Particle Analysis data processing

Except for the 5HT-B and 6HBC-2 dataset, all data were processed using CS-Live to apply motion correction, CTF fitting and initial particle picking[57]. 5HT-B and 6HBC-2 datasets were pre-processed using WARP[58]. Typically, the refined 3D volume from CS-live (or WARP) was used for a homogeneous refinement in cryoSPARC V3.2. 50 2D templates were created from this

refined volume and templated particle picking was performed using these 50 templates. Particles were then extracted at a pixel size of ~2.7 Å/px and 3 *ab initio* models were generated using a subset of 30,000 randomly selected particles. A heterogeneous refinement using the three *ab initio* models and all the extracted particles was then performed. At this point we would have 1 or 2 junk classes and 1 or 2 classes resembling our RNA origami. A non-uniform homogeneous refinement[59] would then be performed using the particles from the good 3D classes. The particles were then re-extracted with adjusted centering of the extraction box based on the aligned particle positions. If the Nyquist resolution was reached or close to being reached, we re-extracted the particles with a bigger box size and less Fourier cropping. These re-extracted particles and the mask from the previous homogeneous refinement were then used as input for 3D variability analysis[60], solving for 3 modes of variability at a filter resolution 2 Å above the resolution attained from the previous homogenous refinement.

We continued particle curation from this point using 2-3 class heterogeneous refinements with the same input volume. After each heterogenous refinement, the highest resolution class was used for a homogeneous refinement and then another round of heterogenous refinement was performed until we reached a point of diminishing return where there was no difference in the heterogeneously refined classes, or until the resolution became worse due to a decreasing particle stack. We found that this method of particle curation produced the best overall maps. However, we were able to produce a map with better local resolution at the most variable kissing loop from the 6HBC-mature dataset by selecting a subset of particles from the 3D variability analysis.

As a last step, we performed local refinement from the last homogeneous refinement, which improved the overall quality of the map as well as the FSC. Local resolution estimation and filtering was also applied within cryoSPARC to adjust the sharpening of the maps and provide a visual representation of the local resolution of the maps. To further improve the best resolved regions of the 5HT-A we created a mask that covered only the three central helices of the origami. A local refinement using this mask resulted in an overall resolution of 3.95 Å and improved density at the crossover and kissing loop regions.

Individual-particle cryo-ET 3D reconstruction of RNA origami satellite

Motion correction was conducted by MotionCor2[61]. The tilt series of whole micrographs were initially aligned by using IMOD[62]. The Contrast Transfer Function (CTF) was determined by the GCTF[63] software package and then corrected by TOMOCTF[64]. Additionally, to reduce the image noise, tilt series were further conducted by a machine learning software, CSBDeep[65], a median-

filter process and a contrast enhancement method. The 3D reconstruction of each individual particle of RNA origami satellite was conducted by the IPET[66] protocol, in which a CTF-corrected tilt series containing a single particle was extracted from the full-size tilt series. This allows us to perform "focused" 3D reconstruction, such that the reconstruction is less sensitive to image distortion, tilt-axis variation with respect to tilt angle, and tilt angle offset. Briefly, each targeted particle was first windowed and then extracted from the whole-micrograph tilt series into a small-size tilt series in the size of 320 × 320 pixel (1.88 Å/pixel). To start the 3D reconstruction, an *ab initio* 3D map was generated as an initial model through back-projecting the small-size tilt series. During the iteration and refinement processes, a set of Gaussian low-pass filter, soft-boundary circular and particle-shaped masks were automatically generated and sequentially applied to the tilt series and projections of the references to increase their signal-to-noise ratio (SNR). To reduce the missing-wedge artifact caused by the limited tilt angle range, the final 3D map were submitted to a low-tilt tomographic 3D reconstruction method (LoTToR)[67]. All IPET 3D reconstructions were low-pass filtered to 60 Å following by Gaussian filtering (standard deviation is 3.0) and median filter (3x3x3) using EMAN software[68] and UCSF Chimera software[69], and displayed by Chimera with application of the hide dust function. The resolution was estimated by two methods. i) Data-to-data based analysis: the FSC between two reconstructed 3D maps from two-halves tilt-series[66] (based on their odd and even tilt index) were generated using IPET aligned particle tilt series. The frequencies at which the FSC curve first falls to values of 0.5 and 0.143 were used to represent the resolution. Notably, the resolution estimated by this method could be severely under-estimated since the reconstructions from the half of tilt-series have a significant lower quality than the final reconstruction. ii) Data-to-model based analysis: the FSC curve between the final IPET reconstruction and the fitting model generated density map was computed, and the frequencies at which the FSC curve fell below 0.5 and 0.143 were used as the estimated resolution. The density map of the fitting model was generated by *pdb2mrc* in EMAN software[68].

Model building

Model building was performed in ChimeraX[69-71]. The NMR structure PDB:2d1b was truncated and fit into the kissing loop regions of the cryo-EM volume as a starting template because comparison of our reconstruction with available KLs from the protein databank revealed the best cross-correlation with the NMR model PDB:2d1b. One might argue that we are biasing our models. However, in the case of the mature 6HB where we consistently observed extra density our 2d1b input model changes to a bulged-out conformation upon real space refinement or

initialization of MDFF simulations. Other helical components were generated for each helical segment using RNAbuild[4], leaving free 5' and 3' ends at the crossover junctions, and then manually positioned into the cryo-EM volume. Once helical placement was approximately correct the individual components were joined using the "make bond" command from the ISOLDE[72] add-on to ChimeraX. The resulting PDB file was re-numbered using the PDB-Tools pdb-reres program[73] and then the correctly numbered PDB file was sequence corrected in ChimeraX using the swapNA command. This model was then passed through real space refinement (RSR) in Phenix[74-76] (using default parameters, our best refined volume and the resolution supplied by the FSC curve at a 0.143 cutoff) to remove any severe clashes that ISOLDE could not handle. The models were then inspected in ChimeraX and subjected to further refinement using Molecular Dynamics Flexible Fitting (MDFF) with VMD using ISOLDE[72]. A final round of RSR in phenix was performed to optimize the backbone angles. Validation of the goodness of fit between model and map were performed using the Phenix validation tool[76-78]. The Phenix RSR and ISOLDE MDFF had comparable cross correlations (CC) to the EM maps but the ISOLDE MDFF produced fewer severe clashes than the Phenix refinement tool, while Phenix produced more usual backbone rotamers at the expense of more clashes.

While the resolution (up to ~4 nm) of IPET 3D reconstructions of the RNA origami satellite is not sufficient to determine the secondary structure of each individual satellite, it is sufficient to shed some light on the domain orientations and positions. This information is useful in revealing the structural heterogeneous and dynamics. 12 density maps were used to build an initial satellite model. This model was used to show the flexibility in angle of bKL by rigid-body docking it into the 12 density maps. During this process, two bKL and one 6HBC of the RNA origami satellite model were separately translated and rotated to fit it to the target position in the density map. As a result, the achieved conformation of the RNA origami satellite had the same domain structure as the initial structure but differed in the relative position and orientation of domains.

Measurements of structural parameters

The torsional angles were extracted from each PDB file using MCQ4 Structures software[79]. Torsion angles for each nucleotide were saved as a CSV file and converted to a JSON Column Array using the convertcsv.com website. The backbone torsions of the nucleotides were analyzed and plotted using a modified R script from Meier *et al.*[80] and shown in Extended Data Fig. 7b.

Helical parameters were measured using the Curves+ software[81,82]. Helical fragments of interest were isolated from the PDB model and renumbered using pdb_reres. Each double stranded

segment was then input into the Curves+ program and the Helical-Rise, Helical-Twist, Major Groove and Minor Groove width parameters were extracted from the resulting .lis file. The helical parameters are listed in Extended Data Fig. 2c.

The angles at and between crossovers were measured using both the density map and the fitted model using orthoscopic view in PyMOL. The crossover θ angle was measured by orienting helices along the x-axis with the junction nucleotides J1-4 in a clockwise orientation running from 5' to 3' (Fig. 2h). The junction is rotated 90 ° about the x-axis to have J2 and J3 on top. The helix axes are now estimated from the density map or the fitted model and the θ angle measured. The measured θ angles are listed in Extended Data Fig. 5c.

The seam curvature φ angle was measured by orienting three helices connected by two crossovers that participate in a seam along the x-axis with the junction nucleotides J1-4 of the two crossovers in a clockwise orientation. The seam was rotated 90 ° about the y-axis to view helices along the helical axis and have J1 and J2 on top. The center of helices are now estimated from the density map or the fitted model in the region close to the crossover and the φ angle measured as the angle between three helix centers. The measured φ angles are listed in Extended Data Fig. 5b.

The seam twist τ angle was measured by orienting three helices connected by four crossovers that participate in two adjacent seams along the x-axis with the junction nucleotides J1-4 of the four crossovers in a clockwise orientation. The seams were rotated 90 ° about the y-axis to view helices along the helical axis and have J1 and J2 on top. The two crossovers of the bottom two helices are aligned based on the fitted model and the τ angle measured as the angle between this crossover and the two crossovers of the top two helices. The measured τ angles are listed in Extended Data Fig. 5d.

Small Angle X-ray Scattering

Samples were measured on an in-house laboratory-based instrument called HyperSAXS[83]. The instrument is an optimized Bruker SAXS NanoStar with a Ga metal jet from Excillum (Kista, Sweden) and home built scatterless slits[84]. The sample was measured continuously in 15 minutes frames for 17.5 hours in total at 25 °C with a concentration of 0.57 mg/mL. The buffer was measured beforehand for 0.5 h and subtracted from each frame using the SUPERSAXS software package (C. L. P. O. and J. S. P, unpublished). This software package was also used to convert data to absolute scale by considering a water sample measured at 20 °C. All SAXS data are plotted as a function of q which is defined as $q = (4\pi\sin(\Theta))/\lambda Ga$, where the scattering angle is defined as

781 2Θ and λGa = 1.34 Å. The transition is visualized by plotting an average of seven data points
782 around the value of q = 0.09 $Å^{-1}$ (0.082-0.10 $Å^{-1}$). A sigmoidal fit is added to guide the eye.
783 The intermediate frames were modelled as a linear combination of the initial and final
784 frame to test if this two-state approximation could describe data. We found that using the first and
785 last frames for the linear combinations, the χ^2 values were not stable over time. Instead, the second
786 and last frames were used, which produced low and stable χ^2 values across the whole series that
787 shows all intermediate frames are well-described by the two-state approximation. For time
788 resolved measurements, it is often necessary to discard the first frame, as there can be small effects
789 from shearing when loading the sample through the tube or changes in temperature.
790 As all intermediate frames can be described well by a linear combination of the initial and
791 mature state, the entire time series can be described by modelling the initial and mature state. First,
792 the program wlsq_PDBx[85] was used to calculate the theoretical scattering curve of the cryo-EM
793 derived structures. These were fitted to data with only the concentration and a constant background
794 as fitting parameters.
795 To improve the fits, Monte Carlo simulations were performed using the structures from
796 cryo-EM. The six individual helixes were separated, and the long helix that kinked in the initial
797 structure was separated in two parts, which gave a total of seven rigid structure elements that could
798 move in relation to each other during the Monte Carlo simulations. The separation of structural
799 elements was done separately using the cryo-EM structure of the initial or mature state. The
800 simulations were run with a low penalty score for clashes to accommodate a broad flexibility of
801 the structures. Ten simulations were run for the initial and mature structure. The program Calc
802 NSD was used to determine the structure that best described the ensemble of the ten individual
803 simulations. A χ^2 value was calculated for each simulation and the average χ^2 value is given with
804 the standard deviation calculated from all ten simulations.
805
806 **Negative stain sample preparation, imaging and analysis**
807 For negative stain the samples were diluted to a concentration of 0.03-0.1 mg/mL. We used ultra-
808 thin carbon film 400 mesh copper grids (CF400-Cu-UL) from Electron Microscopy Sciences for
809 our negative stain TEM work. The grids were glow discharged for 45 seconds at 25 mA using a
810 Pelco easiGlow prior to sample application. 3 uL of sample was applied to the carbon film for 1
811 minute before side blotting on Whatman #1 filter paper and immediate application of 3 uL of
812 Uranyl Formate (5%) solution followed by immediate blotting and reapplication of Uranyl formate
813 for a total of 3 rounds of staining. Grids were then air dried for 10 minutes before imaging.

Images were acquired on a Tecnai Spirit at 120 kV equipped with a TVIPS 4K camera using a pixel size of 1.54 Å/px using Leginon[86] to automate the acquisition of data. The data were saved as 16 bit .tif files and converted to mrc format using EMAN2[87] prior to import into cryoSPARC for image analysis. Micrographs were CTF corrected with Patch CTF within cryoSPARC and curated to remove any bad images. Manual picking was performed for an initial 300 particles that were used to generate templates for templated particle picking. Templated picking resulted in 70,000 particles that were extracted with a box size of 512 pixels downsampled to 128 pixels. 2D classification into 50 classes produced a subset of 18,609 particles in which we could clearly identify the 6HB component and both 5HT wings of the satellite, as well as a single class where the 6HB had landed on its helical axis. These particles were further classified into 50 classes to reveal the conformational heterogeneity of the wing placement. *Ab initio* models lacked sufficient angular distribution of the particles to properly reconstruct the 3D volume, so a 3D template was supplied to enable a better-quality 3D reconstruction to be made.

The specimen of RNA origami satellite was also prepared by optimized negative-staining (OpNS)[88,89]. In brief, an aliquot (4 μl) of the sample was placed on an ultra-thin carbon film grid (CF-200-Cu-UL, Electron Microscopy Sciences, Hatfield, PA, USA) that was prior glow-discharged for 15 seconds. After incubating for 1 min., the excess solution on the grid was removed by filter paper blotting. The grid was then submitted for quickly washing with three droplets of uranyl formate (UF at 1%, w/v) solution. The excess solution of the UF solution was removed by blotting the grid with filter paper from the opposite side of carbon film and then dried under a nitrogen blower. The OpNS EM specimens were examined using a Zeiss Libra 120 Plus TEM (Carl Zeiss NTS, Overkochen, Germany). The instrument was equipped with a LaB_6 gun operating at 120 kV, an in-column energy filter, and a 4 k × 4 k Gatan UltraScan 4000 charge-coupled device (CCD) camera. The un-tilt micrographs were acquired at near Scherzer defocus at a magnification of 80 kX (corresponding to 1.48 Å/pixel). The acquired micrographs were Gaussian high-pass filtered to 400 nm and low-pass filtered to 1 nm.

a

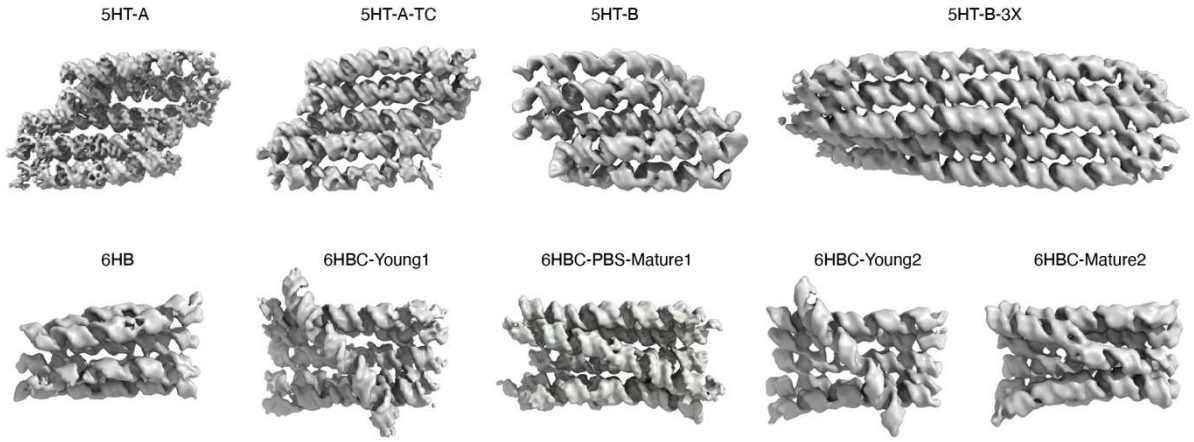

b

Design	Nucleotides	GSFSC resolution	EMD ID	PDB ID	Blueprint / sequence	Cryo-EM Data
5HT-A	544	4.08	13633	7PTQ	Sup. Table 1	Sup. Data 1
5HT-A-TC	548	5.14	13926	7QDU	Sup. Table 2	Sup. Data 2
5HT-B	544	5.71	13636	7PTS	Sup. Table 3	Sup. Data 3
5HT-B-3X	1312	6.50	13592	-	Sup. Table 4	Sup. Data 4
6HB	720	6.61	13627	-	Sup. Table 5	Sup. Data 5
6HBC-Young1	720	5.18	13628	7PTK	Sup. Table 6	Sup. Data 6
6HBC-PBS-Mature2	945	4.90	13630	7PTL	Sup. Table 7	Sup. Data 7
6HBC-Young2	720	7.04	13626	-	Sup. Table 6	Sup. Data 8
6HBC-Mature2	720	7.43	13625	-	Sup. Table 6	Sup. Data 9

Extended Data Fig. 1. Overview of cryo-EM reconstructions of RNA origami designs used in the study. a, Example cryo-EM reconstructions for sheets (top row) and bundles (bottom row). **b**, Table listing RNA origami designs by number of nucleotides, Gold-Standard Fourier Shell Correlation (GSFSC) for the reconstructions, EMD ID, PDB ID and reference to blueprint and sequence.

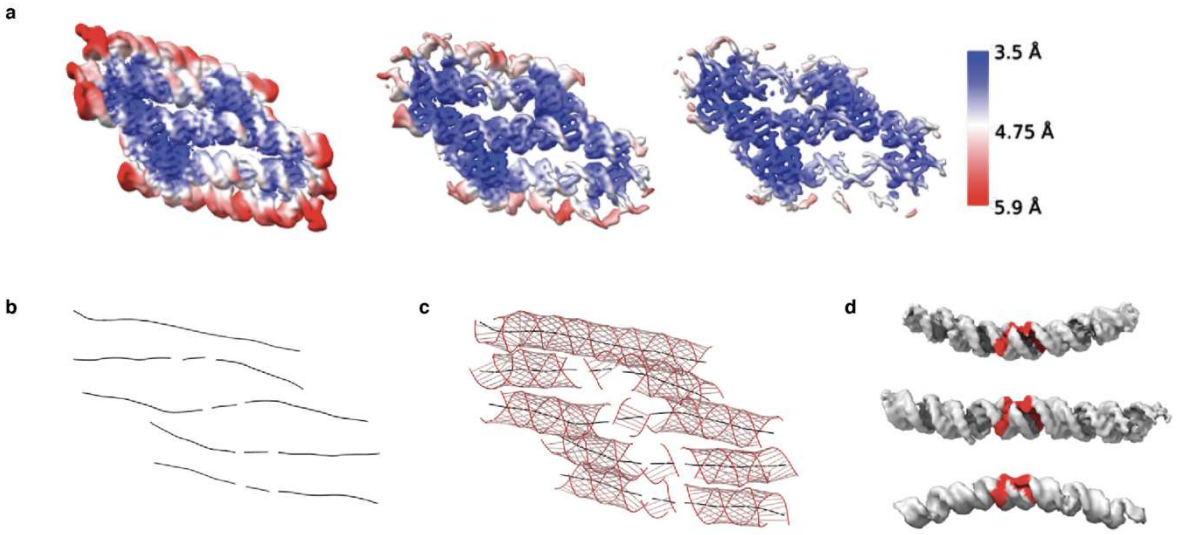

e

Helical regions	Helical Rise (Å/bp)	Helical Twist (°/bp)
All helical regions*	2.7	33.2
KL bases	2.5	31.0
2-bp seams	2.9	35.6
11-bp seam	2.7	32.6
A-form RNA	2.8	32.7

Extended Data Fig. 2. Resolution and Curves+ analysis of 5HT-A model. a, Local resolution estimation from 5HT-A reconstruction shown at levels 0.344, 0.267 and 0.136 from left to right and colour coded by local resolution. **b**, Helical axis shown as black lines. **c**, Backbone shown as red lines with major and minor groove measurements shown as grey lines. **d**, H4 from the 5HT-A (top) and H3 from 5HT-B (bottom) show the most prominent bending; notably, they are bent in opposite directions with respect to the position of A1 and A2 from the KL motif, H3 from 5HT-A (middle) is straight (A1, A2 and A3 positions are shown in red). **e**, Tabulated data from Curves+ analysis of the helical components from the 5HT-A model. * indicates all helical regions except for the KL bases.

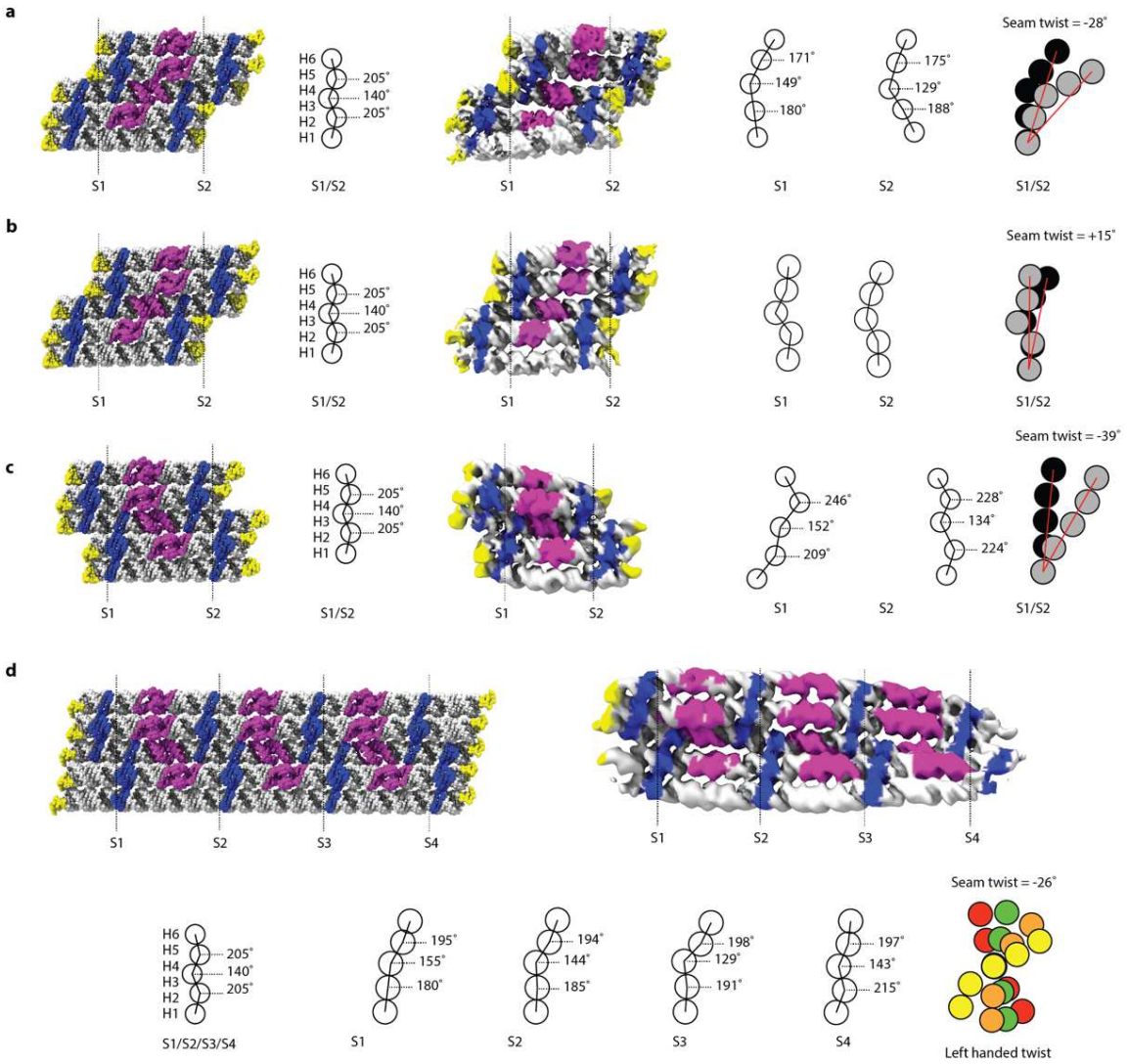

856

857 **Extended Data Fig. 3. Measurements of seam curvature φ angles of 5-helix sheets. a**, 5HT-A
858 ideal model with annotation of seam 1 and 2. Side view show ideal φ angles. 5HT-A cryo-EM map
859 with annotation of seam 1 and 2. Side view show measured φ angles. 5HT-A seam twist
860 measurement. **b**, 5HT-A ideal model with annotation of seam 1 and 2. Side view show ideal φ
861 angles. 5HT-A-TC cryo-EM map with annotation of seam 1 and 2. Side view show measured φ
862 angles. 5HT-A-TC seam twist measurement. **c**, 5HT-B ideal model with annotation of seam 1 and
863 2. Side view show ideal φ angles. 5HT-B cryo-EM map with annotation of seam 1 and 2. Side
864 view show measured φ angles. 5HT-B seam twist measurement. **d**, 5HT-B-3X ideal model with
865 annotation of seam 1 to 4. Side view show ideal φ angles. 5HT-B-3X cryo-EM map with
866 annotation of seam 1 to 4. Side view show measured φ angles. 5HT-B-3X seam twist measurement.

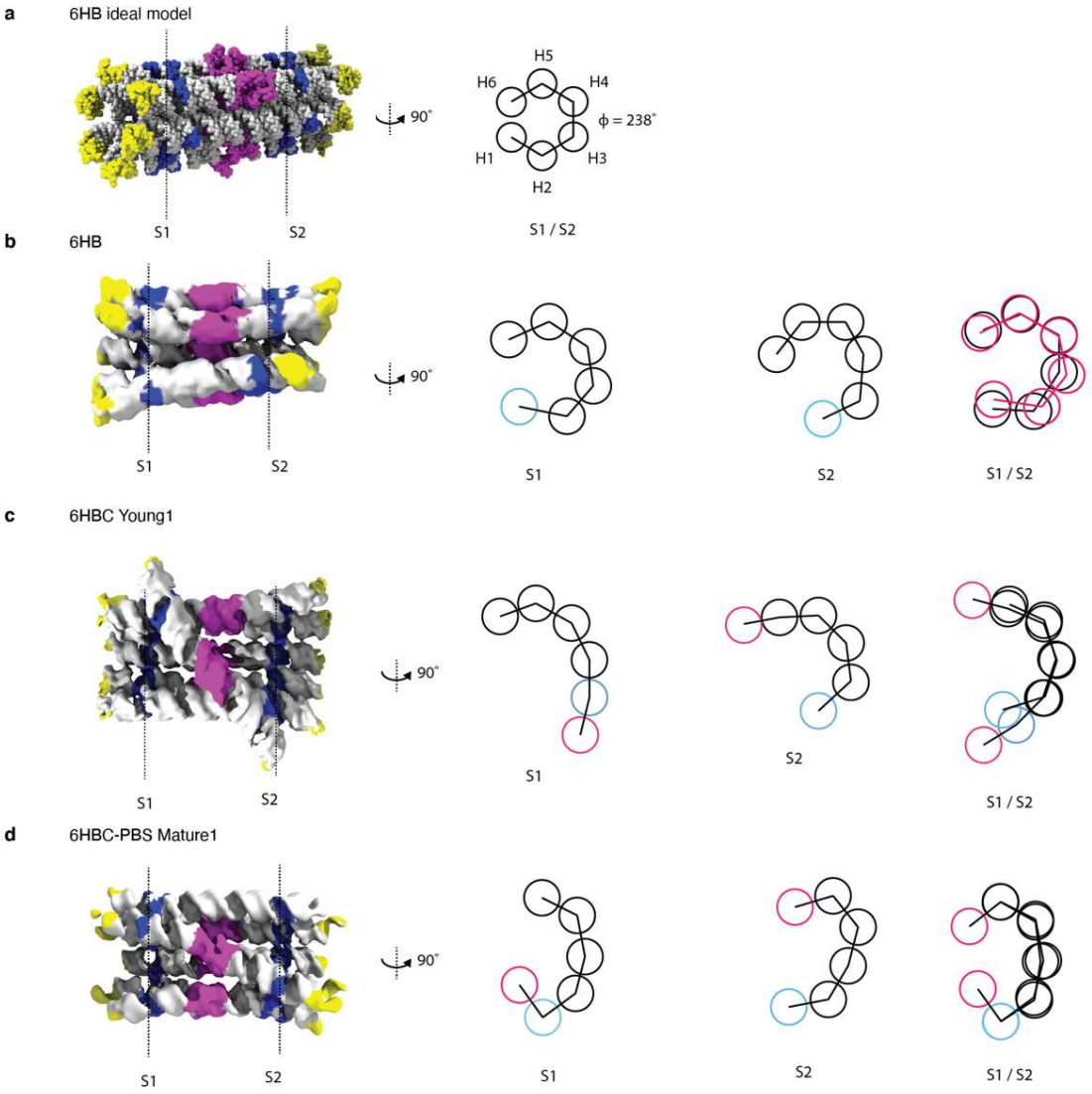

867

868 **Extended Data Fig. 4. Measurements of seam curvature φ angles of 6-helix bundles. a**, 6HB
869 ideal model with annotation of seam 1 and 2. Side view show ideal φ angles. **b**, 6HB cryo-EM
870 map with annotation of seam 1 and 2. Side view show φ angles and seam 1 and 2 and overlay.
871 Helix 1 is colored cyan. **c**, 6HBC-Young1 cryo-EM map with annotation of seam 1 and 2. Side
872 view show φ angles and seam 1 and 2 and overlay. Helix 1 is colored cyan and helix 6 is colored
873 red. **d**, 6HBC-PBS-Mature1 cryo-EM map with annotation of seam 1 and 2. Side view show φ
874 angles and seam 1 and 2 and overlay. Helix 1 is colored cyan and helix 6 is colored red.

a

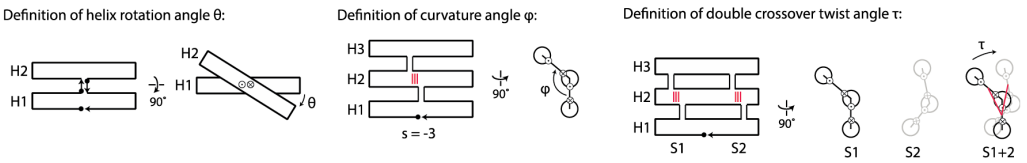

b

Seam name	H1-H2-H3	H2-H3-H4	H3-H4-H5	H4-H5-H6
5HT-A S1	180	149	171	-
5HT-A S2	188	129	175	-
5HT-B S1	209	152	246	-
5HT-B S2	224	134	228	-
5HT-A TC S1	131	242	168	-
5HT-A TC S2	150	230	174	-
5HT-B-3X S1	180	155	195	-
5HT-B-3X S2	185	144	194	-
5HT-B-3X S3	191	129	198	-
5HT-B-3X S4	215	143	197	-
6HB S1	120	131	131	123
6HB S2	120	147	119	123
6HBC-Y S1	166	154	145	131
6HBC-Y S2	126	142	132	173
6HBC-PBS-M S1	90	140	155	128
6HBC-PBS-M S2	132	163	127	113

c

Seam name	H1-H2	H2-H3	H3-H4	H4-H5	H5-H6	H6-H1
5HT-A S1	-26	17	-23	19	-	-
5HT-A S2	21	-23	14	-17	-	-
5HT-B S1	-10	-16	21	1	-	-
5HT-B S2	-3	-3	-19	-10	-	-
5HT-A-TC S1	11	14	-5	18	-	-
5HT-A-TC S2	4	15	18	3	-	-
5HT-B-3X S1	-16	-2	-17	-6	-	-
5HT-B-3X S2	6	-14	-13	0	-	-
5HT-B-3X S3	0	-10	-5	0	-	-
5HT-B-3X S4	4	0	0	0	-	-
6HB S1	-6	-21	8	-9	-8	-
6HB S2	-24	9	-11	3	5	-
6HBC-Y S1	21	-15	9	-14	-	57
6HBC-Y S2	-10	5	-11	12	61	-
6HBC-PBS-M S1	11	-15	21	-14	-	12
6HBC-PBS-M S2	0	15	-16	18	23	-

d

Seam name	H1-H2-H3	H2-H3-H4	H3-H4-H5	Average
5HT-A S1-S2	-17.4	-42.6	-24.0	-28
5HT-B S1-S2	-40.2	-52.8	-24.2	-39
5HT-A-TC S1-S2	+7	+17	+20	+15
5HT-B-3X S1-S2	-8.9	-44.2	-14.1	-22
5HT-B-3X S2-S3	-53.3	-27.1	-13.4	-31
5HT-B-3X S3-S4	+11.0	-40.7	-47.4	-26
6HB S1-S2	-29.5	+5.0	-9.0	-22.0
6HBC-Y S1-S2	-12.4	-22.5	-35.6	-
6HBC-PBS-M S1-S2	-7.1	-7.2	+6.0	-

Extended Data Fig. 5. Measurement of structural parameters. a, Definitions of angles. **b**, Seam curvature φ angles measured on cryo-EM maps and models. **b**, Crossover θ angles measured on cryo-EM maps and models. **c**, Seam twist τ angles measured on cryo-EM maps and models. Each row in the table corresponds to a seam of a given RNA origami structure. The seams (S) are numbered from 5' to 3' and helices (H) are numbered from helix 1, which contain the transcription start site, as shown in Supplementary Table 1-8. Each column refers to the two helices defining the crossover angle θ.

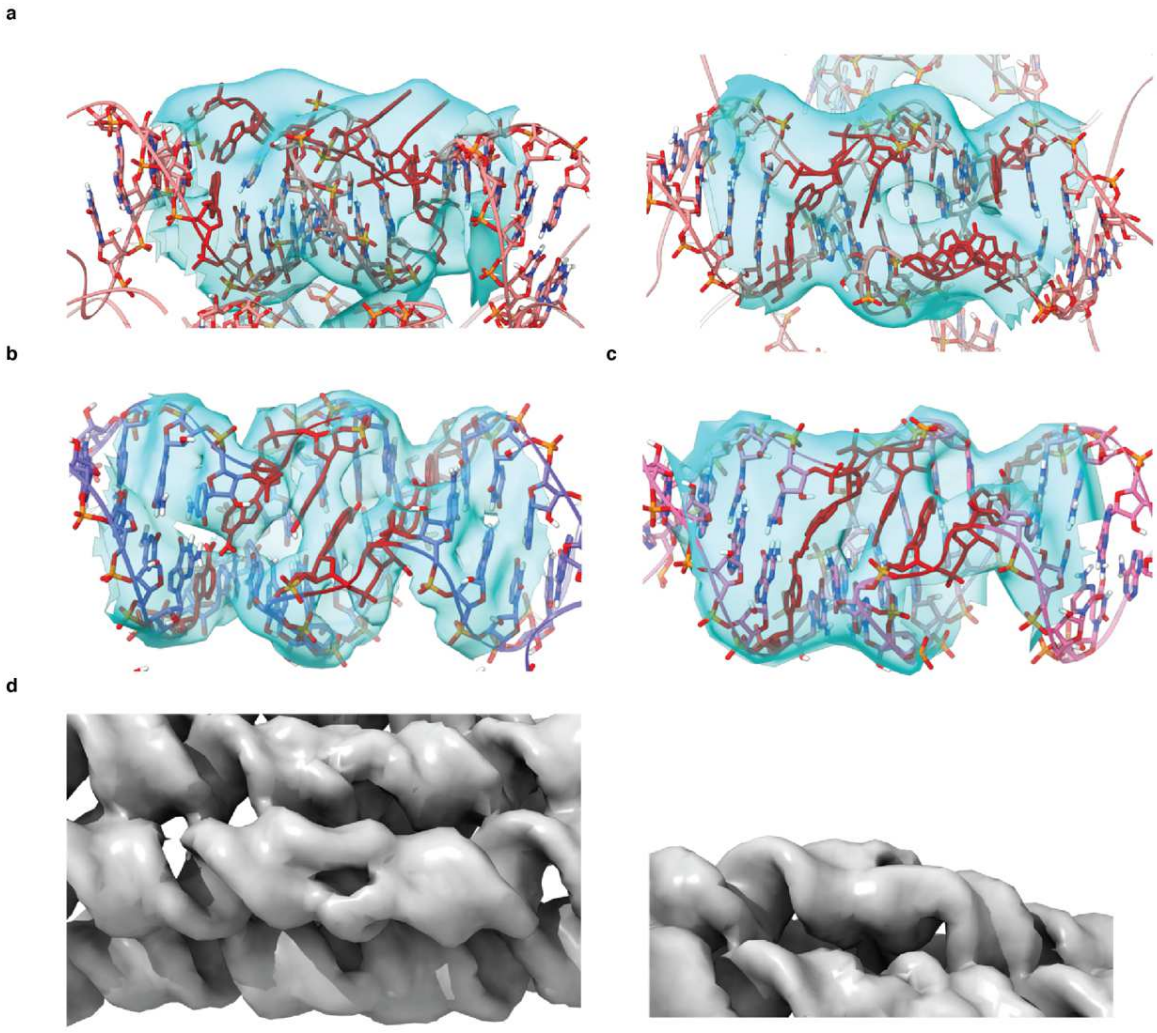

Extended Data Fig. 6. Comparison of KL regions and position of adenines. a, Two views of the instance of bulged out adenines from our 6HBC-mature dataset. A notable protrusion is present where the adenines are modeled, and a clear lack of density is in the spot where density from base stacking adenines is observed in our highest resolution 5HT-A dataset **b** and our lower resolution 5HT-B dataset **c**. Adenines shown in red against coulomb potential map shown in cyan. **d**, A similar gap in density was observed in helix 3 of the 6HB no clasp reconstruction. Left image shows top view. Right image shows side view.

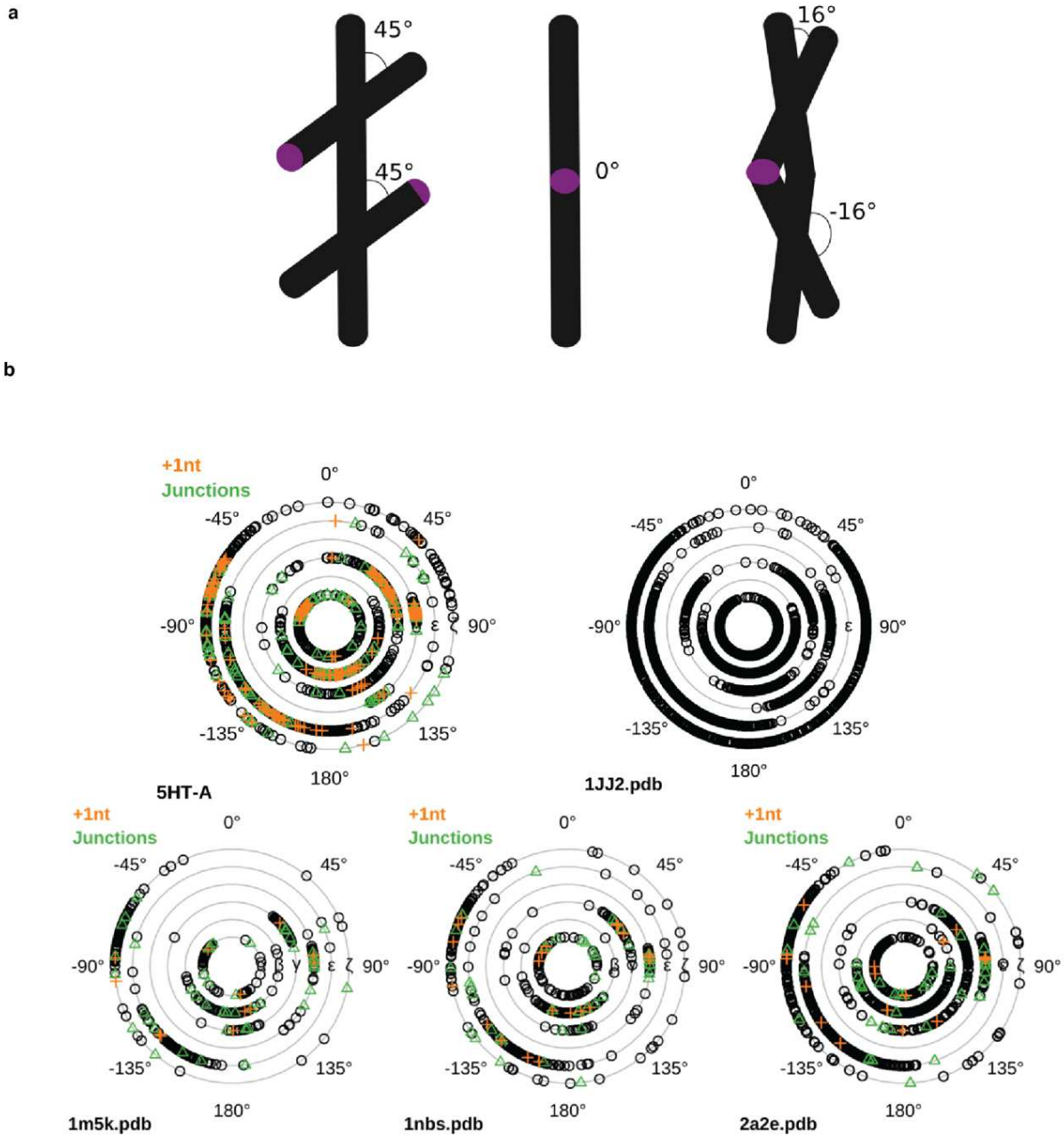

Extended Data Fig. 7. Crossover θ angles and backbone torsion angles. a, Cartoon showing the relaxed crossover θ angle (left), our predicted double crossover θ angle (middle) and the observed double crossover θ angle (right), kissing loop regions are depicted in magenta. **b**, Torsion angles for the 5HT-A model compared to the torsion angles observed in the ribosome (1J32) and in other RNA with antiparallel crossovers (1m5k, 1nbs, 2a2e). The seven rings from inner to outer represent the alpha, beta, gamma, delta, epsilon and zeta angles, respectively. Nucleotides at the crossover junction are shown in green and nucleotides adjacent to the junction are shown in orange, all other nucleotides are shown in black.

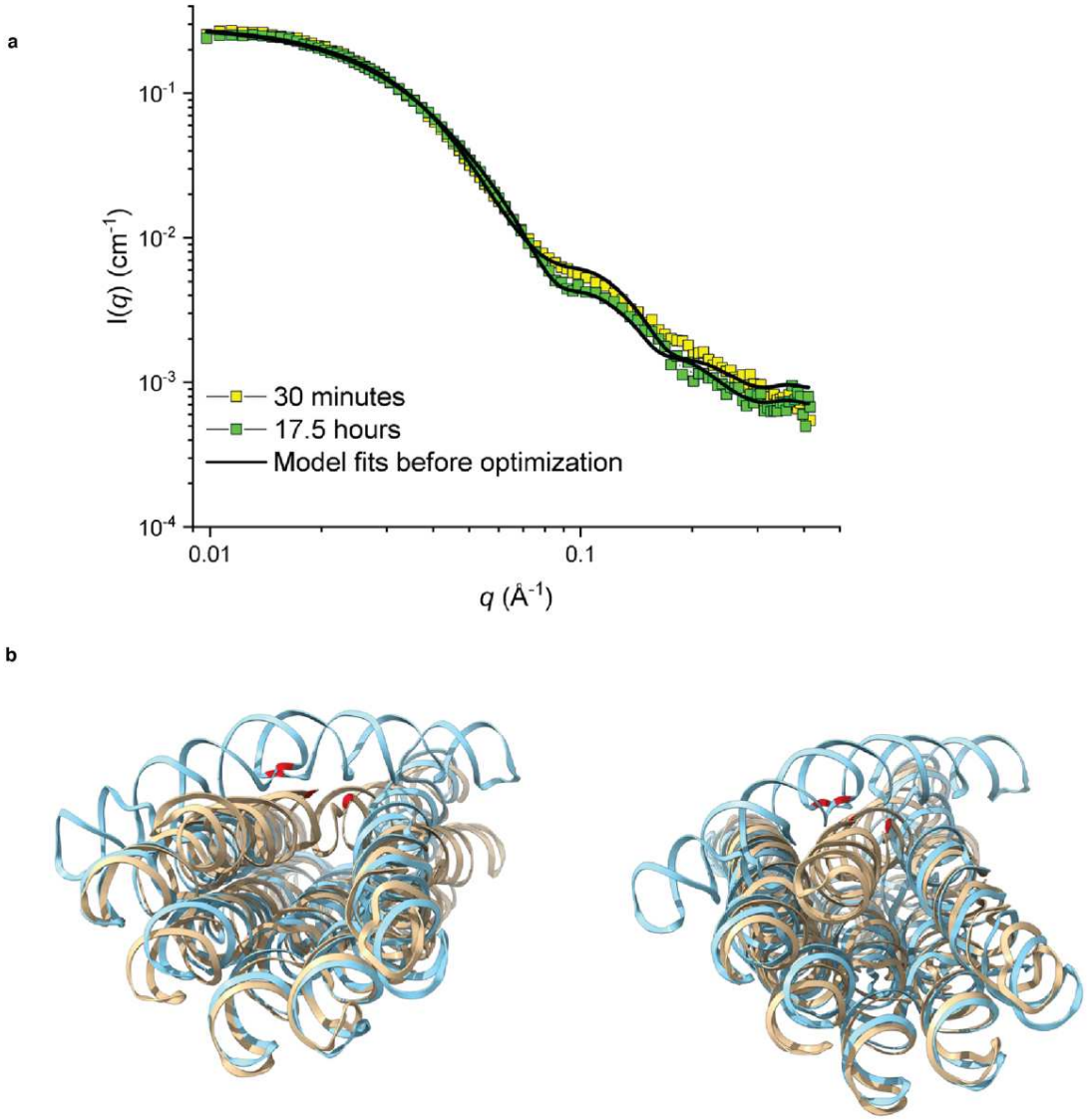

900

901 **Extended Data Fig. 8. SAXS data and model fitting. a**, SAXS data showing observed scattering
902 pre and post structural transformation of the 6HBC and the predicted scattering from the models
903 prior to rigid-body minimization. **b**, Two views of an overlay of the two conformations (young
904 and mature are turquoise and beige, respectively) of the 6HBC with the cross strand adenine base
905 stack shown in red.

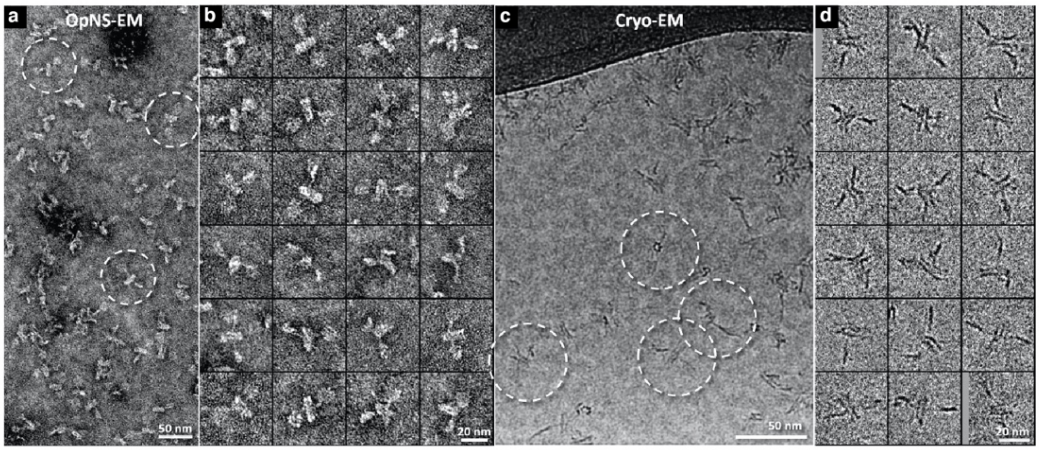

Extended Data Fig. 9. TEM images of 16H-Satellite RNA. a, Optimized-negative stain (OpNS) TEM micrograph and **b** representative particles of the 16H-Satellite RNA; **c**, cryogenic TEM micrograph and **d** representative particles of the 16H-Satellite RNA.

a

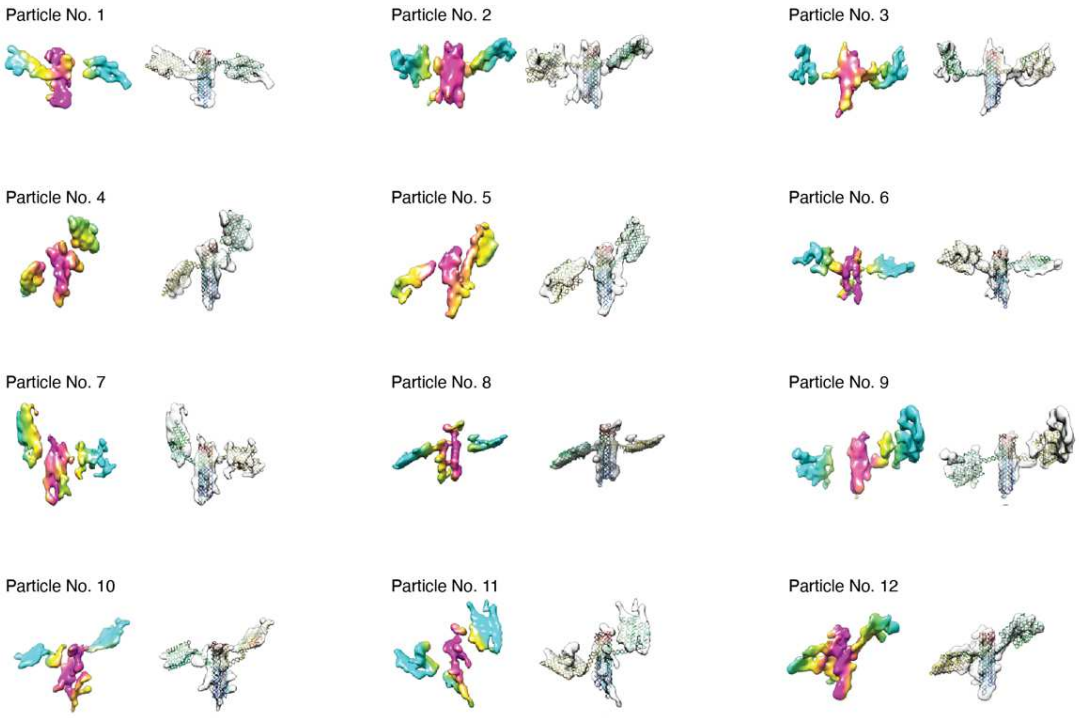

b

Particle	Map vs. map		Map vs. model		EMD ID	Cryo-ET Data
	FSC 0.5 / Å	FSC 0.143 / Å	FSC 0.5 / Å	FSC 0.143 / Å		
No. 1	124	60	52	37	25078	Sup. Data 15
No. 2	120	80	94	78	25080	Sup. Data 16
No. 3	130	64	78	33	25081	Sup. Data 17
No. 4	177	92	64	34	25082	Sup. Data 18
No. 5	206	55	80	53	25083	Sup. Data 19
No. 6	356	70	90	43	25084	Sup. Data 20
No. 7	106	38	69	35	25085	Sup. Data 21
No. 8	171	41	44	32	25086	Sup. Data 22
No. 9	92	38	80	33	25087	Sup. Data 23
No. 10	169	88	43	34	25088	Sup. Data 24
No. 11	226	44	62	32	25089	Sup. Data 25
No. 12	170	61	111	51	25090	Sup. Data 26

Extended Data Fig. 10. IPET 3D reconstruction of an individual particles of 16HS. a, 12 particles shown as the final 3D density map and map superimposed with the flexible docked model. **b**, Table listing FSC analyses of the final map resolution by two methods, the "map vs. map" and "map vs. model". Four resolutions were measured respectively based on two criteria (the frequencies of FSC curve falls at 0.5 and 0.143, respectively).

Supplementary Files

This is a list of supplementary files associated with this preprint. Click to download.

- 20211217McRaeSupplementaryMaterials.pdf
- Video1.mp4
- Video2.mp4
- Video3.mp4
- Video4.mp4